
Article:
Allan, ASR, Barker, SJ, Millet, M-A et al. (2017) A cascade of magmatic events during the assembly and eruption of a super-sized magma body. Contributions to Mineralogy and Petrology, 172. 49. ISSN: 0010-7999

https://doi.org/10.1007/s00410-017-1367-8

A cascade of magmatic events during the assembly and eruption of a super-sized magma body

Aidan. S.R. Allan[1], Simon J. Barker[1,2], Marc-Alban Millet[1,3], Daniel J. Morgan[4], Shane M. Rooyakkers[1,5], C. Ian Schipper[1], Colin J.N. Wilson[1*]

[1]School of Geography, Environment and Earth Sciences, Victoria University of Wellington, P.O. Box 600, Wellington 6140, New Zealand

[2]School of Environment, University of Auckland, PB92019, Auckland 1142, New Zealand

[3]School of Earth and Ocean Sciences, Cardiff University, Cardiff CF10 3AT, UK

[4]School of Earth and Environment, University of Leeds, Leeds LS2 9JT, UK

[5]Department of Earth & Planetary Sciences, McGill University, Montreal, Quebec H3A 0E8, Canada

Manuscript for: *Contributions to Mineralogy and Petrology*

*Corresponding author: email: colin.wilson@vuw.ac.nz

Revised version: 9 May 2017

Abstract

We use comprehensive geochemical and petrological records from whole-rock samples, crystals, matrix glasses and melt inclusions to derive an integrated picture of the generation, accumulation and evacuation of 530 km^3 of crystal-poor rhyolite in the 25.4 ka Oruanui supereruption (New Zealand). New data from plagioclase, orthopyroxene, amphibole, quartz, Fe-Ti oxides, matrix glasses, and plagioclase- and quartz-hosted melt inclusions, in samples spanning different phases of the eruption, are integrated with existing data to build a history of the magma system prior to and during eruption. A thermally and compositionally zoned, parental crystal-rich (mush) body was developed during two periods of intensive crystallisation, 70 and 10-15 kyr before the eruption. The mush top was quartz-bearing and as shallow as ~3.5 km deep, and the roots quartz-free and extending to >10 km depth. Less than 600 yr prior to the eruption, extraction of large volumes of ~840 °C low-silica rhyolite melt with some crystal cargo (between 1 and 10%), began from this mush to form a melt-dominant (eruptible) body that eventually extended from 3.5-6 km depth. Crystals from all levels of the mush were entrained into the eruptible magma, as seen in mineral zonation and amphibole model pressures. Rapid translation of crystals from the mush to the eruptible magma is reflected in textural and compositional diversity in crystal cores and melt inclusion compositions, versus uniformity in the outermost rims. Prior to eruption the assembled eruptible magma body was not thermally or compositionally zoned and at temperatures of ~790 °C, reflecting rapid cooling from the ~840 °C low-silica rhyolite feedstock magma. A subordinate but significant volume (3-5 km^3) of contrasting tholeiitic and calc-alkaline mafic material was co-erupted with the dominant rhyolite. These mafic clasts host crystals with compositions which demonstrate that there was some limited pre-eruptive physical interaction of mafic magmas with the mush and melt-dominant body. However, the mafic magmas do not appear to have triggered the eruption or controlled magmatic temperatures in the erupted rhyolite. Integration of textural and compositional data from all available crystal types, across all dominant and subordinate magmatic components, allows the history of the Oruanui magma body to be reconstructed over a wide range of temporal scales using multiple techniques. This history spans the tens of millennia required to grow the parental magma system (U-Th disequilibrium dating in zircon), through the centuries and decades required to assemble the eruptible magma body (textural and diffusion modelling in orthopyroxene), to the months, days, hours and minutes over which individual phases of the eruption occurred, identified through field observations tied to diffusion modelling in magnetite, olivine, quartz

and feldspar. Tectonic processes, rather than any inherent characteristics of the magmatic system, were a principal factor acting to drive the rapid accumulation of magma and control its release episodically during the eruption. This work highlights the richness of information that can be gained by integrating multiple lines of petrologic evidence into a holistic timeline of field-verifiable processes.

Keywords

Oruanui eruption, Taupo volcano, rhyolite, magma chamber, magma accumulation, eruption timings

Introduction

The nature and generation of large silicic magma bodies

The study of large silicic eruptions and their parental magmatic systems offers many challenges. One central issue is determining whether the processes and timescales involved in the generation of small volumes of evolved magma are the same as for the accumulation of vast magma bodies that feed supereruptions (i.e. $>10^{15}$ kg or ~450 km^3 magma: e.g. Self 2006). Do large bodies of eruptible magma take longer to be generated than smaller ones (e.g. Smith 1979; Shaw 1985; Reid 2008; de Silva and Gregg 2014), or do they accumulate on similar timescales, driven by processes with faster rates (e.g. Wilson and Charlier 2009; Gualda et al. 2012a; Wotzlaw et al. 2015)? By extension, questions arise as to how such vast volumes of melt-rich magma can accumulate without erupting, what controls the lifetime of eruptible magma bodies and, what triggers eruption onset (e.g. Gregg et al. 2012; Gelman et al. 2013; Caricchi et al. 2014a; Malfait et al. 2014; Myers et al. 2016)?

Answers to these questions are sought either by numerical modelling (e.g. Jellinek and DePaolo 2003; Bachmann and Bergantz 2004; Huber et al. 2011, 2012) or geochemical and petrological investigation of eruption products (e.g. Girard and Stix 2010; Gualda et al. 2012a); the latter approach having the advantage of directly linking to hard evidence in the field (e.g. Wilson et al. 2006; Wilson and Charlier 2009; Allan et al. 2012, 2013; Bain et al. 2013). Petrological studies can be controversial (particularly in the case of the Bishop Tuff), as it is essential to interpretations of petrological data to determine if crystals grew together *in situ* over a definable range of intensive variables (Hildreth 1979; Gualda et al. 2012a, b; Evans and Bachmann 2013; Chamberlain et al. 2015), or if they are aggregated from a wide

range of sources (e.g. Eichelberger 1978; Gamble et al. 1999; Dungan and Davidson 2004; Davidson et al. 2005). Furthermore, it is desirable for multiple co-erupted crystal phases to be considered together (e.g. Hildreth 1979; Girard and Stix 2010; Chamberlain et al. 2014a, 2015). Although useful information can be recovered from studies of single phases (e.g. Bishop Tuff quartz – Peppard et al. 2001; Wark et al. 2007; Thomas et al. 2010; Gualda et al. 2012a, Pamukcu et al. 2012, 2016; Gualda and Sutton 2016) there is a risk of introducing unintended systematic bias.

The crystal archive in crystal-poor ignimbrites

The crystal mush model (e.g. Brophy 1991; Hildreth 2004; Bachmann and Bergantz 2004, 2008; Bachmann and Huber 2016) provides a widely utilised framework with which to explore large crustal bodies of silicic magma. The mush itself has generally been envisaged as a largely un-eruptible body of viscous material (Smith 1979), and numerical modelling has focussed on determining how mush bodies might 'defrost' and/or remobilise (Burgisser and Bergantz 2011; Huber et al. 2010, 2011). Mafic magma is often implicated in supplying the heat and volatiles required to mobilise the mush to drive voluminous eruptions of crystal-rich magma (e.g. Parmigiani et al. 2014). However, the origins and rates of accumulation of crystal-poor rhyolites, which are generally thought have been extracted from mush zones, are potentially widely diverse (Bachmann and Bergantz 2008; Bachmann and Huber 2016 for overviews).

Two considerations from the crystal mush model pertain to the origins of crystal-poor rhyolites. (1) Large volumes of evolved melt may be available for extraction from a mush zone at any given point in time. (2) If crystal-poor rhyolite does originate from a crystal-rich reservoir, crystal-melt segregation on a massive scale is required at some stage prior to eruption. It is not yet known if such large scale segregation leaves a tangible record of this process in the small fraction of crystals that are actually erupted and, if so, how such records could be used to temporally and physically constrain these events. A further complication is that any signals recorded in crystals of events related to melt body generation must be deconvoluted from subsequent growth in the eruptible magma. This last point raises questions of which crystals are phenocrystic (grown in the melt with which they were erupted), antecrystic (derived from consanguineous parental sources), or xenocrystic (foreign to the magma in which they are found) (Bacon and Lowenstern 2005; Charlier et al. 2005). It is also possible that a given crystal may contain domains attributable to all three origins (e.g. Charlier et al. 2008).

In this paper we document the timing and mechanisms of pre- and syn-eruptive magmatic processes for the Oruanui eruption (Taupo, New Zealand). We integrate new and published major- and trace-element analyses of whole-rock samples, matrix glasses, crystals, and quartz- and plagioclase-hosted melt inclusions (see Table S.1), for both the volumetrically dominant rhyolites and subordinate co-erupted mafic magmas. We explore the textural and compositional relationships within and between crystal phases, to provide a summary of the magmatic processes and their associated timescales that operated during the establishment, assembly and eruption of the super-sized Oruanui magma body.

The Oruanui eruption

Eruption summary

The Oruanui eruption at 25,360 ± 160 (2 sd) cal yr BP (Vandergoes et al. 2013) from Taupo volcano in the central North Island of New Zealand (Fig. 1) is the youngest supereruption on Earth, discharging ~530 km^3 of moderate- to high-silica rhyolite magma with 3 to 13 wt % crystals (Wilson 2001; Wilson et al. 2006). Ten eruptive phases are identified, based on bedding and grading characteristics in the fall deposits. The eruption was episodic, with several time breaks varying in duration from probably only hours (i.e. long enough for the eruption plume to have dispersed and ash to wholly settle out before the next phase began), to a period of months between phases 1 and 2 during which time reworking and bioturbation of the earlier ash occurred (Wilson 2001). Extensive interaction of magma with lake water during the eruption caused rapid chilling, extensive fragmentation and produced extremely widely dispersed, fine-grained fall deposits and a large, non-welded ignimbrite (Self and Sparks 1978; Self 1983; Wilson 2001; Van Eaton et al. 2012; Van Eaton and Wilson 2013). The eruption products are fresh, glassy and entirely non-welded, although pumices large enough for detailed study are largely restricted to the ignimbrite. The interbedded nature of the fall deposits and ignimbrite, and spikes in the abundance of juvenile mafic material, allow the eruption phase boundaries to be linked between the fall and flow deposits (Wilson 2001), such that clasts sampled from the ignimbrite can be placed within a time-stratigraphic context.

Juvenile products

Juvenile products of the Oruanui eruption fall into seven categories (five felsic, two mafic; Table 1). By far the most voluminous, comprising ~98% of the total erupted volume, is highly vesicular white pumices of high-SiO_2 rhyolite (HSR hereafter), defined as having whole-rock SiO_2 >74 wt%. HSR clasts characteristically contain 3-13 % crystals, have quartz forming 9-21 % of the crystal fraction and mostly have more orthopyroxene than amphibole (opx 45-82% to amph 55-18%: Sutton 1995 in Wilson et al. 2006). Sparse (~0.5 %), white, low-SiO_2 rhyolite pumices (LSR, whole-rock compositions <74 wt% SiO_2) lack quartz and have more amphibole than orthopyroxene (opx 29-42% to amph 71-58%; Ibid.). Wilson et al. (2006) originally considered HSR and LSR to represent a compositional continuum, but Allan et al. (2013) inferred that they were separate entities (see also Results section below) that only encountered each other syn-eruptively. We focus on these two of the rhyolite types in this paper.

Three additional, volumetrically minor (<< 1 %) but genetically significant Oruanui rhyolitic components have previously been identified, and are summarized here for completeness. The first is pumices showing a white/pale grey streaky nature, and which fall along a mixing trend between the HSR and more mafic magma (Sutton 1995; Wilson et al. 2006, figure 18). The second is pumices that show enrichment in MgO for a given SiO_2, and have been similarly attributed to mixing of HSR and more mafic magma but the clasts show no signs of mingling in hand specimen (Sutton 1995; Wilson et al. 2006, figure 18). The third is a denser, more crystal-rich, biotite-bearing rhyolite pumice, identified as a 'foreign' magma sourced from the nearby but wholly chemically and isotopically independent 'NE dome' system (Sutton et al. 1995; Fig. 1). This biotite-bearing magma is interpreted to have been fed laterally by diking from its parental magma system into the Oruanui conduit at the onset of eruption and throughout phases 1 and 2 (Allan et al. 2012), but it has not been identified in later eruption products.

Clasts of juvenile mafic magma from two physically and chemically distinct lineages also occur within the Oruanui deposits: an olivine-bearing calc-alkaline group and a tholeiitic group in which olivine is very rare. Based on detailed componentry of ash-grade material from the eruption deposits (Wilson 2001), the two mafic lineages together are estimated to represent 3-5 km^3 of magma. The relative proportions of the calc-alkaline to tholeiitic end-members are not constrained, although subequal numbers of clasts from each type have been collected. The mafic clasts are inferred to be juvenile on the basis of cauliform or crenulated margins, indicating that they were hot and plastically deforming until quenched on eruption (Wilson 2001; Rooyakkers 2015 and manuscript in preparation). The two mafic groups are

compositionally distinguished on plots of whole-rock SiO_2 versus FeO_t/MgO with both calc-alkaline and tholeiitic groups being almost entirely contained within the appropriate fields as defined by Miyashiro (1974).

Samples studied

For this study, we collected HSR pumices from early-erupted fall deposits (phases 1 and 2); and from early (phases 2 and 3), mid- (phase 7) and late-erupted (phase 10) ignimbrite within the stratigraphic framework of Wilson (2001). Wilson et al. (2006) showed that, although there was notable compositional variability within the Oruanui rhyolites, the deposits themselves were not systematically zoned with respect to stratigraphic height (Fig. S.1). The melt-dominant magma body, accordingly, was inferred to have undergone thorough mixing at some stage prior to eruption (Wilson et al. 2006). The LSR pumices were sampled from phase 3 ignimbrite at a single location (at the Hinemaiaia C Dam in Lake Taupo Forest: locality 1086 of Wilson 2001), where LSR material was previously observed to be most abundant.

Analytical techniques

Whole rock analytical methods

To expand the data set in Wilson et al. (2006), single clasts of rhyolitic (Allan et al. 2012, 2013, this study) and mafic compositions (this study) were analysed for their bulk chemistries by X-ray fluorescence (XRF) and solution ICP-MS techniques. Clasts were cleaned to remove any adhering matrix, soaked overnight in de-ionised water, and placed in an oven at 110 °C until dry. The mafic clasts, which commonly contained thin adhering rinds of white rhyolite, were coarsely crushed using an agate mortar and pestle, so that fragments of rhyolite could be picked out prior to powdering to ensure characterisation of the mafic end-member. The clasts were then reduced to powder using an agate mill. Whole-rock major element oxide compositions were determined by XRF by either Spectrachem Analytical (CRL Energy LTD, Wellington, New Zealand) or the late Dr John Watson at the Open University, UK. International rock standards BHVO-2 (USGS, Hawaiian basalt), BCR-2 (USGS, Columbia River basalt), and JR1 (GSJ, rhyolite) were analysed during the same sessions at Spectrachem, and WSE (Whin Sill dolerite) and OU-3 (Nanhoron microgranite) at the Open University. Data for the first three standards are summarised in the supplementary material of Allan et al. (2013), and for the two Open University standards in the supplementary material

(Table S.2) for this paper. Overall, relative differences from accepted values are BHVO-2: <2 % except for MnO (-11%) and P_2O_5 (11%); BCR-2: <2% except for MnO (-10%), Na_2O (-2.5%) and P_2O_5 (5.7%); JR-1: <2 % except for TiO_2 (-3.7%), MnO (-11.5%), MgO (23%) and K_2O (5.4%); WSE: <1%; OU-3: < 1% except for MnO (1.7%), CaO (4.5%) and Na_2O (1.6%). Overall relative 2 sd precisions are better than 1 % for SiO_2, Al_2O_3 and Fe_2O_3, 1-2% for MnO, MgO, CaO, Na_2O and P_2O_5, and 3-5% for K_2O and TiO_2.

Whole-rock trace element compositions were determined using an Agilent 7500CS ICP-MS and Thermo Scientific Element2 sector-field ICPMS at Victoria University of Wellington. Sample and standard powders were digested using conventional HF + HNO_3 methods. Calculation of trace element concentrations were determined from raw count rates, after correction for off-peak zeros, by reference to the known elemental concentrations of the BHVO-2 whole-rock standard, and utilising ^{43}Ca as the internal standard with the CaO content of samples previously determined to ~ 1% by XRF. Standards BCR-2, BHVO-2 and JR-1 were analysed under identical conditions and during the same analytical sessions as the Oruanui rhyolitic (Allan et al. 2012) and mafic samples (this study). Data for these standards are available in the online supplementary information of Allan et al. (2012). Overall, relative differences from accepted values are BHVO-2: <1% except for Zn (-5.7%), Tm (1.1%) and Lu (1.4%); BCR-2: <5%, except for Cr (-16%) and Mo (25%); JR-1: <5% except for Yb (5.2%), Er (6.6%), Zr (-7.7%), Ti (-8.6%), Gd (8.6%), Ho (9.2%), Sc (14%), V (-29%), Cr (-40%), Mo (-75%), Zn (78%) and Cu (150%). Average % 2 sd precisions based on analysis of whole rock standards are < 3% (MgO, TiO_2, V, Ga, Rb, Sr, Y, Zr, Nb, La); 3 to 5% (MnO, Ba, Ce, Pr, Nd, Sm, Eu, Gd, Tb, Dy, Ho, Er, Tm, Yb, Lu, Hf, Th, U); 5 to 10% (Cu, Pb); 10 to 15% (Sc, Mo, Cs); 15 to 20% (Zn).

In-situ analytical methods

Crystals were liberated from the host felsic clasts by gently crushing in an agate mortar and pestle, then hand-picked from the appropriate size fraction and mounted in epoxy resin blocks. Analysis of crystals from the mafic clasts was approached in two ways. (1) Crystals were handpicked from the 0.5 to 1.0 mm size fraction of crushed material and mounted in epoxy resin blocks. (2) Clasts were thin sectioned so that mineral phases at sizes <0.5 mm could be imaged and analysed within their host groundmasses. All *in situ* analyses of glass and mineral phases considered here (Allan et al. 2012, 2013, and new data) were undertaken using a JEOL JXA-8230 electron probe microanalyser (EPMA), and a New Wave 193 nm laser ablation system coupled to an Agilent 7500CS ICP-MS at Victoria University of

Wellington. Glass analyses by EPMA were conducted at an accelerating voltage of 15 kV and current of 8 nA with the beam de-focused to 10 μm and count times for Na reduced to minimise the effects of alkali-loss. Mineral analyses by EPMA were conducted at 12 nA under a focused electron beam (~2 μm). Prior to *in-situ* analysis of the HSR and LSR mineral phases, high resolution back-scattered electron (BSE) images of each crystal were obtained. These images were used to note crystal textures and zonation features and infer, where possible, a crystal stratigraphy to ensure that at least the inferred oldest and youngest, and most- and least-evolved, domains of each crystal were targeted for analysis. Standardisation was determined using a series of natural and synthetic standards, chosen to match as closely as possible the matrix composition of the material being analysed. Secondary mineral standards (Engels amphibole, Johnstown hypersthene, NMNH 115900 plagioclase, Kakanui augite, Springwater olivine) and glass standards (ATHO-G, VG-A99, VG-568) were analysed throughout the analytical sessions to monitor signal stability and inform estimates of precision and accuracy.

Trace element analyses by LA-ICP-MS included a minor isotope of a major element (typically ^{29}Si or ^{43}Ca), previously determined by EPMA for use as an internal standard (Pearce et al. 1996). For analysis of the ferromagnesian mineral phases, the USGS basaltic glass standard, BHVO-2G, was used as the calibration standard, whereas NIST612 was used for analysis of plagioclase and melt inclusions. The ICP-MS was tuned by adjusting the positions of the torch, lenses, and the inflow of ultra-pure He while rastering at 2 μm/sec across the calibration standard. Data for samples and standards were collected under identical conditions during 60 s acquisitions (plus 60 s for backgrounds), under a static laser beam of 25 to 35 μm diameter, and pulsed at 5 Hz. Analytical data were reduced using the Iolite software package using the trace element (Internal Standard) data reduction scheme (Hellstrom et al. 2008). The raw time-resolved signal from each analysis was scrutinised to identify and remove any data compromised by the accidental ablation of contaminant (non-targeted) phases, before final trace element contents were calculated. Estimates of precision and accuracy of LA-ICP-MS data were derived from repeat analyses of the glass standards BHVO-2 (USGS Hawaiian basalt), BCR-2G (USGS, Columbia River basalt) and ATHO-G (MPI-DING, Icelandic rhyolite) and are given in supplementary material Table S.3. Overall, relative differences from accepted values are BHVO-2G: <5% except for Sc (-5.7%), Ni (5.6%), Cu (36%), Zn (-9.0%), Tm (-7.1%) and W (-9.0%); BCR-2G: <5%, except for Sc (5.4 %), Mn (6.6%), Ni (-7.4%), Cu (-21 %), Zn (11%) and W (18%); ATHO-G: <10%

except for Mg (17%), Sc (140%), Ti (13%), V (-12%), Cr (-51%), Cu (-15%), Ga (-19%) and Cu (17%). Average % 2 sd precisions based on analysis of glass standards are

- BHVO-2G: <10% (Li, Mg, Sc, Ti, V, Mn, Co, Zn, Ga, Rb, Sr, Y, Zr, Nb, Ba, La, Ce, Pr, Nd, Eu, Tb, Dy, Hf, Ta, Th), 10-20% (Ni, Sm, Gd, Ho, Er, Tm, Yb, Pb, U) and >20% (Cu, Cs, Lu, W);
- BCR-2G: <10% (Li, Mg, Sc, Ti, V, Mn, Co, Zn, Ga, Rb, Sr, Y, Zr, Nb, Ba, La, Ce, Pr, Nd, Eu, Tb, Dy, Ho, Er, Hf, Th, U), 10-20% (Cr, Ni, Sm, Gd, Tm, Yb, Lu, Ta, Pb) and >20% (Cu, Cs, W);
- ATHO-G: <10% (Li, Mg, Mn, Ga, Rb, Sr, Y, Zr, Nb, Ba, La, Ce, Pr, Nd, Tb, Dy, Ho, Er, Yb, Hf, Pb, Th, U), 10-20% (CaO, Sc, Ti, V, Zn, Sm, Eu, Gd, Tm, Lu, Ta, W) and >20% (B, Cr, Co, Ni, Cu, Cs).

Results

Oruanui rhyolite compositions

Whole rock and glass chemistry

Whole-rock rhyolite compositional data are presented in Wilson et al. (2006) and Allan et al. (2013), and a representative suite of the latter data is given in Table 2. A compilation of all existing and new data for the juvenile mafic clasts is in Electronic Appendix 1 and a representative suite of new data given in Table 3. HSR pumices have relatively uniform glass compositions, but all LSR clasts have bimodal glass compositions (Electronic Appendix 2; Fig. 2a). The more evolved of these is compositionally identical to the HSR matrix glass, and glass from the widespread Oruanui fall deposits (Lowe et al. 2008; Allan et al. 2008; Vandergoes et al. 2013; Table S.4). The presence of the two, non-hybridized glass populations has been interpreted to reflect latest-stage entrainment of HSR melt into LSR magma, immediately prior to quenching (Allan et al. 2013). Quartz-hosted melt inclusion data presented here (Electronic Appendix 2) confirm observations by Liu et al. (2006) and Bégué et al. (2015) that inclusions in HSR samples are more evolved than the groundmass glass (Fig. 2b). Although there is some overlap, these data indicate that for at least part of their history most Oruanui quartz crystals grew from (and trapped) melts that were more evolved than the carrier melts in which they were erupted (i.e., quartz is largely xenocrystic relative to the groundmass pumice glass). The LSR glass data from both plagioclase-hosted melt inclusions and groundmass glass forms two trends when Rb/Sr is plotted against Ti

content:, one with a steeper, higher Ti array, and the other a shallower, lower Ti array (Fig. 2d) along trends towards less-evolved compositions.

Textural linkages between crystal phases in the HSR

Backscatter electron (BSE) images of amphibole, pyroxene, plagioclase and Fe-Ti oxides, and cathodoluminescence [CL] images of quartz, reveal textural and zonation features in the main crystal phases, particularly in those of the volumetrically dominant HSR. Allan et al. (2013) noted that ~90% of HSR orthopyroxene showed distinctive core-rim relationships, in which a more Mg- and inclusion-rich core was surrounded by 40-400 μm thick inclusion-poor rim that was normally zoned with a consistent $En_{46\pm2}$ composition in its outermost parts (Fig. 3a). Zonation in individual crystals varies due to combined effects of dissolution and recrystallisation, unequal kinetic/growth zonation and overprinting from Fe-Mg interdiffusion (Allan et al. 2013). The remaining ~10% of HSR orthopyroxenes tended to be inclusion-poor and lacked any significant core-rim zonation.

BSE images of individual HSR plagioclase crystals show that they record a complementary suite of textures to the orthopyroxenes. In total, 89% of the HSR plagioclase crystals (n = 168) also have prominent core-rim zonation (Fig. 3b). The cores are typically truncated by at least one episode of resorption and are surrounded by subhedral to euhedral overgrowths that are normally zoned towards an outermost composition of $An_{38\pm2}$. Of these zoned crystals, 48% have cores that are patchy/sieve textured, and 41% show significant resorption but no evidence of sieve texturing (Fig. 3b); and they can be further subdivided into those with high An (>An_{70}) cores, and those with prominent blue-grey cores (e.g. Charlier et al. 2008). The remaining 11% of HSR plagioclase are either nominally unzoned (An contents varying by <3 mol%, and accounting for ~7% of all HSR plagioclase), or showed normal, oscillatory zonation with no distinction between core- or rim-zones.

The HSR quartz textures in CL images indicate a history that is not directly comparable to those of the plagioclase and orthopyroxene (Fig. 4). Brightness of quartz under CL scales with Ti concentration (Peppard et al. 2001; Wark et al. 2007; Matthews et al. 2012). The causes of varying or oscillating concentrations of Ti in magmatic quartz are debated around fluctuations in temperature (e.g. Wark and Watson 2006; Wark et al. 2007), pressure (Thomas et al. 2010, 2015; Huang and Audétat 2012), and/or the combined influences of temperature, pressure and melt compositions (Wilson et al. 2012). Regardless of the ultimate controls on CL (≈Ti) zonation in quartz, the Oruanui HSR quartz crystals do

not follow an overarching zonation pattern. Some quartz crystals have darker cores and brighter rims, and others show the opposite. Many crystals are multiply-zoned with many bright and dark bands, yet some are devoid of any CL zonation at all. In direct contrast to the plagioclase and orthopyroxene, the outermost quartz rims do not appear to converge on a consistent zonation pattern or composition. This is consistent, however, with the analytical data in Liu et al. (2006) and Wilson et al. (2012), where quartz rim analyses show roughly the same mean (~85 ppm) and as wide a range of Ti concentrations (~50 to 120 ppm) as the dataset as a whole, implying that mixing in of quartz crystals from a variety of sources occurred.

Compositional characteristics of crystals in the HSR and LSR

A new suite of mineral analyses has been undertaken for this work to supplement the data in Wilson et al. (2006) and provide the basis for our revised interpretations. Full data sets are presented in Electronic Appendices.

Plagioclase. HSR plagioclase crystals (Electronic Appendix 3) have a wide range of anorthite contents from An_{26} to An_{88} , mostly reflecting diverse crystal core compositions (Fig. 5a). The majority of crystal rims, however, converge on a narrow range of $An_{38\pm2}$. The majority of crystal cores and interiors have compositions that are less evolved (57% are $An_{>42}$), and a minority that are more evolved (12% are An_{26-35}) than the rims. Texturally homogeneous grains (unzoned in BSE imagery) cluster in their composition around those of the rim compositions of the other grains. The LSR plagioclase crystals (Fig. 5b) exhibit a more restricted range of compositions, the majority (94%) ranging between An_{38} and An_{60}. The outermost rims of LSR plagioclase are relatively restricted in composition with 91 % of analyses in the range $An_{44\pm6}$. The LSR plagioclases show steep positive or negative trends between An content and Sr (Fig. 5c) and Ba (Fig. 5d). The same parameters for the HSR crystals show two limiting trends in the cores and interiors data that converge around the compositions of the outermost rims.

Orthopyroxene. Major and trace element compositional data for both HSR and LSR orthopyroxenes (after Allan et al. 2013: Electronic Appendix 4) show similar ranges (Fig. 5e-h), with the biggest difference being that the outermost HSR rims grains show a very restricted compositional range (95% are $En_{46\pm2}$), whereas the outermost LSR rims are generally more variable. HSR orthopyroxene rims have very uniform Al contents, whereas HSR cores and interiors have a significant tail-off to higher Al values. The LSR

orthopyroxenes show a similar compositional range to the HSR crystals, but in general a greater proportion of them are in the higher Al range. Ti and Al trend positively with En content, whereas Mn and Zn are anti-correlated with Al (Fig. 5e-h). Overall, there are no major compositional differences between the fields of HSR and LSR orthopyroxenes.

Amphibole. The majority of HSR outermost rim compositions (Electronic Appendices 5 and 6) are tightly clustered (47 ± 1 wt% SiO_2, 1.4 ± 0.2 wt% TiO_2, 7 ± 1 wt% Al_2O_3, 12 ± 1 wt% MgO) (Fig. 6). The data from HSR cores plus interiors and LSR amphiboles overlap this range but also extend to higher concentrations of TiO_2 and MgO (Allan et al. 2013). The amphibole Eu/Eu* ratio was used by Allan et al. (2013) as a first-order proxy for melt composition, with higher Eu/Eu* values indicating growth from lesser evolved melts and vice versa. Allan et al. (2013, their figure 3) reported that concentrations of Mn and Zn show an initial increase with decreasing Eu/Eu* but then their abundance decreases below Eu/Eu* of ~0.45. Similar noteworthy inflections in the abundances of Eu (going from static to decreasing abundances: Fig. 6b), and Ni and Co (going from static to increasing abundances: Fig. 6c,d) are also evident around this same hinge point. Eu/Eu* ratios of the amphiboles are linearly and positively correlated (R^2 of 0.83: Allan et al. 2013) with the apparent pressures of amphibole crystallisation derived from the calibration of Ridolfi et al. (2010). The abundances of elements such as Mn, Eu, Ni and Co when plotted against model pressures suggest that changes in amphibole chemistry occurred once the amphiboles crystallised at model pressures of <140-160 MPa, equivalent to depths of ~6 km.

Intensive variables

Estimates of Oruanui magma intensive variables and water contents have been made through a variety of measurements and models. The results of preferred thermometric models, i.e. those that gave realistic, consistent and reproducible temperature estimates, are summarised in Table 4 and Fig. S.2. Analytical data for Fe-Ti oxides are given in Electronic Appendix 7. Application of the Ghiorso and Evans (2008) model (using the EPMA correction factors from Evans et al. 2006) to equilibrium pairs (after Bacon and Hirschmann 1988) yielded mean temperatures of 790 °C and 840 °C for the HSR and LSR magmas, respectively. The same Fe-Ti oxide pairings applied to the Sauerzapf et al. (2008) model yield temperatures ~15 to 25 °C higher. Despite the offset between the two Fe-Ti oxide models, both indicate a ~40 to 50 °C difference between the final pre-eruptive temperatures of the HSR and LSR magmas.

419 The compositions of outermost amphibole rims for the HSR and LSR magmas, using
420 the Si* parameter of Ridolfi et al. (2010, equation 1), yielded mean temperatures of 784 °C
421 and 843 °C, respectively. However, both rhyolite groups are skewed by a subordinate
422 component of crystal rims that tail off to higher temperatures. Prominent model temperature
423 modes centre on ~ 770-780 °C (HSR rims) and ~830 °C (LSR rims: Table 4; Fig. S.2). The
424 plagioclase-melt and orthopyroxene-melt thermometers of Putirka (2008, equations 24a and
425 28a, respectively), were applied to the compositions of outermost crystal rims (Allan et al.
426 2013) and matrix glass. Plagioclase-melt and orthopyroxene-melt thermometry yielded mean
427 estimates of 787 °C and 785 °C, respectively, for HSR samples, and mean estimates of 831
428 °C and 830 °C, respectively, for LSR samples.
429 Estimates of the final pressures for storage and crystallisation of the Oruanui rhyolites
430 were determined using the total-Al based formulation of Ridolfi et al. (2010; their equation 4)
431 applied to outermost amphibole rim compositions (Fig. S.3). Based on these compositions
432 only, HSR samples yielded a mean model pressure of 113 MPa (range 88 to 185 MPa), with a
433 prominent mode between 90 and 120 MPa. The mean model pressure for LSR amphibole
434 rims was 174 MPa (range 114 to 243 MPa). As with the HSR amphiboles, the mode of the
435 estimates is slightly lower than the mean. These amphibole-derived pressures for the HSR are
436 consistent with those estimated from concentrations of H_2O and CO_2 in trapped quartz-hosted
437 melt inclusions (Liu et al. 2006) which have a mean pressure of 138 MPa (range 94-188
438 MPa). Broadly similar pressure estimates were also presented by Bégué et al. (2014), using
439 rhyolite-MELTS compositions from Oruanui [HSR] quartz-hosted melt inclusions.
440 Estimates of the final oxygen fugacity for the HSR and LSR magmas were calculated
441 using amphibole rim compositions (Ridolfi et al. 2010; their equation 2), and Fe-Ti oxide
442 equilibrium pairs (Ghiorso and Evans 2008; Sauerzapf et al. 2008) (Table 5). Use of the
443 Ghiorso and Evans (2008) model for Fe-Ti oxides in HSR clasts yields a mean estimate of -
444 0.2 NNO, compared to a mean of +0.47 NNO when the Sauerzapf et al. (2008) model is used.
445 The Ridolfi et al. (2010) formulation applied to amphibole rims yields a mean value of +0.9
446 NNO. Mean oxygen fugacity calculated for the LSR samples were as follows: -0.1 NNO
447 (Ghiorso and Evans 2008, model); +0.4 NNO (Sauerzapf et al. 2008); +0.5 NNO (Ridolfi et
448 al. 2010).
449 Measurements and estimates of the mean water content of the Oruanui HSR magma
450 vary from 4.5 wt% to 6.2 wt% (Table 5). The lowest values come from FTIR measurements
451 of H_2O in quartz-hosted melt inclusions (Liu et al. 2006). The higher estimates are inferred
452 from amphibole rim compositions (Ridolfi et al. 2010; their equation 3), empirical modelling

453 of H_2O solubility applied to Oruanui HSR compositions (Moore et al. 1998) and plagioclase-
454 melt equilibrium models (Housh and Luhr 1991; Waters and Lange 2015).
455
456 **Oruanui mafic compositions**
457 *Whole rock chemistry*
458 Mafic clasts analysed in here and previously (Wilson et al. 2006; Rooyakkers 2015) range
459 between 50-65 % SiO_2, in distinct tholeiitic (higher Fe, Ti) and calc alkaline (lower Fe, Ti)
460 groups (Fig. 7a; Table 3). New trace element data show that many of the mafic clasts notably
461 have Eu/Eu* values around or greater than 1 (Fig. 7b).
462
463 *Compositional characteristics of crystals in mafic clasts*
464 As previously stated, *in-situ* analysis of crystal phases from the mafic clasts was approached
465 in two ways, either on hand-picked separates, or from thin sections of slabbed material. In
466 general the sectioned samples contain greater proportions of smaller-sized and more primitive
467 crystals (higher En orthopyroxene, lower SiO_2 amphibole, higher An plagioclase). The
468 distribution of the data sets for sectioned clasts (analysed by EPMA only) versus handpicked
469 separates (EPMA + LA-ICP-MS) in Fig. 8 highlights that the trace element dataset for
470 crystals from the mafic clasts may under-represent the abundance of less-evolved crystals as
471 an artefact of the crystal size fraction used for LA-ICP-MS analysis. Plagioclase data appear
472 to be most affected by this apparent sampling bias, with no plagioclase from mafic clasts with
473 FeO_t contents greater than 0.5 wt % having been analysed by LA-ICP-MS (Fig. 8b). It is also
474 apparent that most of the major element compositional ranges in the larger crystals fall
475 entirely within the compositional fields defined by the corresponding crystal species in the
476 HSR and LSR rhyolites. Linkages between plagioclase textures and major element
477 chemistries show several features (Fig. 9). The majority of analyses that returned high Fe
478 contents at a given An content were almost exclusively analyses on groundmass plagioclase
479 (microlites) or from very thin (<5 μm) quench crystallisation rims on larger crystals (see also
480 Rooyakkers 2015 and manuscript in preparation). Of the plagioclase crystals that are
481 consistent with derivation from the rhyolites (i.e. overlapping the compositional fields for
482 HSR and LSR crystals), most show thin rims that increase markedly in BSE brightness (i.e.
483 higher An) reflecting their late-stage immersion in hotter, more mafic melt compositions
484 (e.g. CA_P919 plag 16 in Fig. 9). Others have thicker (>100 μm) rim zones of mottled high

485 An surrounding relatively featureless more sodic cores (e.g. CA_P987 plag 2 in Fig. 9),
486 possibly indicating a more prolonged exposure to mafic magma.
487 Olivines from calc-alkaline clasts are almost entirely unzoned with respect to BSE
488 imagery and major element composition, and returned uniform compositions of $Fo_{85\pm1}$
489 (Electronic Appendix 8). However, the outermost rims of these olivines had very thin (<5
490 μm) BSE-brighter, more Fe-rich rims of Fo_{74}. Olivine is rare in the tholeiitic clasts but three
491 examples gave compositions between Fo_{75} and Fo_{65}. Rare clinopyroxene crystals ranged from
492 En_{34} to En_{49} and Wo_{32} to Wo_{44} (Electronic Appendix 8). The trace element compositions of
493 plagioclase, orthopyroxene and amphibole from the mafic clasts fall almost entirely within
494 the corresponding HSR and LSR crystal fields making identification of crystals considered to
495 be phenocrystic in the mafic magmas difficult (Figs. 10 and S.4). Notable exceptions to this
496 in the calc-alkaline clasts are the very high-An plagioclase (An_{85-95}), and in the tholeiitic
497 clasts the high-En orthopyroxenes and some of the least evolved amphiboles (Eu/Eu* >~0.8).
498
499 *Intensive variables*

500 Constraining magma intensive variables in the Oruanui mafic magmas is challenging because
501 the compositional and textural data indicates that many of the crystals in the mafic clasts are
502 not equilibrium phases. Of the models and phases available to constrain pre-eruptive
503 temperatures, Fe-Ti oxides may be considered the most appropriate because they are known
504 to re-equilibrate very rapidly at magmatic temperatures (typically days to weeks; e.g. Freer
505 and Hauptman 1978; Hammond and Taylor 1982; Venezky and Rutherford 1999).
506 Temperatures calculated from equilibrium pairs (after Bacon and Hirschmann 1988) of Fe-Ti
507 oxides from the mafic samples return bimodal temperature estimates centred around 1000 °C
508 and 840 °C (Fig. 11). This bimodality suggests that there are Fe-Ti oxides from both the
509 mafic and rhyolitic end-members in the mafic clasts. We do not use the Ridolfi et al. (2010)
510 thermobarometric formulations for the mafic amphiboles because the larger crystals are
511 clearly inherited from the rhyolite and the groundmass amphiboles are inferred to have grown
512 under disequilibrium conditions during rapid crystallisation (Rooyakkers 2015). Two-
513 pyroxene thermometry has been applied by pairing together clinopyroxene (inferred to be
514 phenocrystic) and the most primitive orthopyroxenes (i.e. those with compositions that are
515 only found in the mafic clasts). When only pairings that pass the Fe-Mg exchange
516 equilibrium test of Putirka (2008) (i.e. $K_D = 1.09 \pm 0.14$) are used, average temperatures of

~1010 °C or 1038 °C are calculated using the Brey and Kohler (1990) and Putirka (2008) models, respectively (n=19: Fig. 11b).

Discussion

The diversity of crystal textures and compositions presented in this study highlights the wide range in magma compositions and intensive conditions within the pre-eruptive Oruanui magmatic system. Wilson et al. (2006) demonstrated that although there was significant whole-rock compositional diversity in the Oruanui rhyolitic clasts, there were no systematic changes in composition with respect to eruption phase (i.e. stratigraphic height: Fig. S.1), and therefore no systematic zonation within the immediately pre-eruptive Oruanui melt-dominant magma body. This is confirmed by HSR crystal rims that converge to uniform compositions for each eruptive phase, whether the earliest (phase 1) or latest (phase 10) or vented from different areas within what became the Oruanui caldera (Fig. S.5). Below we consider a sequence of events that led to this final uniformity from what was originally a diverse magma reservoir, and examine factors that governed the development, storage and evacuation of the 530 km^3 Oruanui melt dominant magma body.

Generation of the Oruanui melt-dominant magma body from a zoned crystal mush

On the basis of amphibole and orthopyroxene textural and chemical data, combined with P–T–H_2O constraints, Allan et al. (2013) proposed that the Oruanui HSR magma body had accumulated following rapid decompression and extraction of large volumes of melt (plus entrained crystals) from a crystal-rich mush-like source body. The significant decompression event is reflected in the *in-situ* chemistry of amphibole cores and interior zones which were interpreted to record a chemical signature of the dissolution-recrystallisation history that is texturally evident in orthopyroxene crystals (Fig. 3a). Orthopyroxene destabilisation occurred during decompression from as much as 270 MPa to ~140 MPa, and is recorded in the amphiboles as increasing levels of Mn and Zn, two elements notably enriched in the orthopyroxenes and inferred to have been taken up in the amphiboles as the orthopyroxenes dissolved (Fig. 6a). Decompression to less than ~140 MPa saw the re-stabilisation and re-growth of orthopyroxene rims and a decrease in the abundance of Mn and Zn in the co-crystallising amphiboles.

New data presented here for plagioclase crystals further supports the interpretation of rapid extraction and melt accumulation. The significant resorption ± sieve texturing of ~90%

550 of the plagioclase cores, followed by overgrowths of rim-zones (Fig. 3b) are inferred to
551 represent a disequilibrium-then-regrowth history parallel to that experienced by 89% of the
552 orthopyroxenes (Fig. 3). The presence of resorption zones and raddled cores in the feldspars
553 could represent a decompression event or interaction with hotter, less evolved melts within
554 the mush zone, including those parental to the erupted mafic clasts. Experimental studies on
555 andesitic compositions have shown that sieve-textures similar to that observed in the HSR
556 plagioclase cores can form in response to rapid decompression under fluid-undersaturated
557 conditions (Nelson and Montana 1992). Detailed consideration of the blue-grey-cored
558 plagioclases by Charlier et al. (2008; Fig. 3b) showed that these cores had been partially
559 resorbed, then interacted with hotter melts (including those of metasedimentary crustal
560 origin) to yield dusty textures (cf. Tsuchiyama 1985) in some cases before overgrowth of
561 rims zoned out to the common $An_{38\pm2}$ range. A general origin for the raddled cores through
562 rapid growth is unlikely because these cores span a wide variety of compositions, indicating
563 that their original growth occurred under a variety of conditions, and the inclusions cross-cut
564 the growth zones, indicating that they are a superimposed feature (cf. Nelson and Montana
565 1992). The notable decrease in the abundance of Eu in the amphiboles at ~140 MPa is
566 commensurate with the inflection of Mn concentrations (Fig. 6a, b) that Allan et al. (2013)
567 interpreted to reflect the re-stabilisation and re-growth of orthopyroxene upon reaching the
568 accumulating melt-dominant magma body. The decrease in Eu content of the amphiboles
569 may similarly reflect the restabilisation and crystallisation of plagioclase in the melt-
570 dominant magma body following the decompression experienced by the host magma parcel.
571 A common magmatic history can therefore be inferred for the majority of plagioclase,
572 orthopyroxene and amphibole crystals in the HSR clasts: derivation from a deeper, hotter and
573 less evolved source mush, followed by entrainment and crystallisation of rim-zones in the
574 cooler, shallower and more evolved melt-dominant magma body. The earlier history of HSR
575 quartz crystals, however, contrasts with that inferred for these other main phases, with the
576 trapped melt inclusions recording more evolved compositions than the final (HSR) melt-
577 dominant magma body. Crystallisation of the quartz rim-zones took place in the melt-
578 dominant magma body, along with plagioclase, orthopyroxene and amphibole, as shown by
579 the close correspondence between compositions of the host melt (i.e. groundmass glass) and
580 those of re-entrant inclusions (Liu et al. 2006).
581 Allan et al. (2013) highlighted the significant compositional overlap between the
582 earlier-grown portions of the HSR crystals (i.e. cores plus interiors) and whole crystals from
583 the LSR, in addition to overlapping P-T conditions indicated by amphibole compositions.

584 They argued that the LSR magma, seen as discrete clasts ejected during the eruption in only
585 minor proportions, in fact approximated the initial composition of the voluminous crystal-
586 poor magmas extracted from the crystal mush/source zone. The hundreds of cubic kilometres
587 of this magma that were extracted then, following crystallisation of the rim-zones on many
588 crystals and associated cooling of the order of 40-50 °C, culminated in the final HSR
589 composition. This is consistent with the findings of Wilson et al. (2006), that the HSR
590 compositions could be generated from LSR compositions following ~ 28% fractionation of
591 the crystal phases recorded in the pumices. In this light, the LSR pumices that were sampled
592 during the eruption itself are considered to represent isolated bodies of crystal-poor rhyolite
593 magma that existed in the crystal-mush source reservoir, and that were syn-eruptively tapped
594 during evacuation of the HSR magma body (cf. Cashman and Giordano 2014). Allan et al.
595 (2013) noted that all LSR clasts examined were quartz-free and that quartz may have only
596 begun to grow in the melt-dominant magma body after the melt had evolved to SiO_2-
597 saturated conditions. The short (decades to centuries) timescales proposed from melt
598 inclusion faceting in the Oruanui quartz by Pamukcu et al. (2015) thus only reflect a part of
599 the physical and chemical evolution of the magma body. In light of the expanded crystal-
600 specific dataset considered here, we review these approaches in order to more fully explain
601 some of the features of quartz and the other crystal phases discussed above.
602
603 **A revised model for the pre-eruptive development of the Oruanui magma body**
604 The diversity of compositions and inferred P-T conditions determined from the crystal cores
605 and interiors reflect earlier derivation of the crystals from a thermally and compositionally
606 zoned crystal-mush source. During the processes of crystal-liquid separation, large volumes
607 of melt plus entrained crystals were carried upwards into the melt-dominant magma body that
608 was forming at shallow crustal levels (~90-140 MPa, or ~3.5-6 km depth). Convection and
609 stirring of the accumulating melt-rich body destroyed any compositional stratification (cf.
610 Bishop Tuff: Hildreth and Wilson 2007; Chamberlain et al. 2015) and resulted in melt
611 homogenization that generated compositionally uniform crystal rims. Quartz-hosted melt
612 inclusions (indicating crystal growth from more evolved melts during the formation of the
613 crystal interiors, to slightly less-evolved conditions in the main melt-dominant magma body:
614 Fig. 4; Liu et al. 2006, also Bégué et al. 2015) indicate that quartz was only stable in the
615 uppermost layers of the mush body prior to melt segregation. The interstitial melt in this part
616 of the mush was highly evolved (on the basis of Rb/Sr ratios) and the modal values from

volatile saturation pressures (Liu et al. 2006) indicate that this zone was at pressures of ~120 to 150 MPa (~4.5-5.5 km depth) but not greater than ~190 MPa (>7 km depth). Compositional characteristics of melt inclusions in sparse CL-dark quartz cores observed by Liu et al. (2006) and age characteristics of inherited zircons in post-Oruanui eruptives (Charlier et al. 2010; Barker et al. 2014) are consistent with at least part of this mush being an intrusive remnant of the 350 ka Whakamaru magma systems (Brown et al. 1998; Matthews et al. 2012). It thus seems likely that some of the plagioclase (e.g., those with compositions notably more evolved than the outermost rims), amphibole and orthopyroxene co-crystallised with quartz in this upper part of the mush layer. Similarly, a small component of the amphibole cores and interiors have low-Al compositions that may reflect their earlier growth and crystallisation from evolved interstitial melt in the quartz-bearing portion of the mush. Quartz is absent in the post-Oruanui rhyolites (Barker et al. 2015), which are typically 20-60 ˚C hotter than the Oruanui magma, supporting the inference that quartz was only stable in the upper and cooler parts of the pre-Oruanui mush.

Downward thermal and compositional stratification of the mush below the quartz-bearing zone is reflected in the compositions of plagioclase (increasing An content: Fig 5a-d) and orthopyroxene (increasing En content: Fig 5e, f). The amphibole compositions reflect increasing model temperatures with depth in the mush pile, reaching ~920 °C at pressures of ~270 MPa or ~10 km depth, with corresponding compositional gradients reflected in co-related Eu/Eu* values (Allan et al. 2013: Fig. 6). In addition, the plagioclase compositional data from the HSR clasts show evidence for two contrasting sources for the An>50 plagioclase cores (Fig. 5). A subordinate population has somewhat depleted concentrations of compatible elements (e.g. Sr, Mg; Figs. 5c) and elevated levels of incompatible elements (e.g. Ba, Pb: Fig 5d) at values of An >50. Although these particular cores have bulk compositions that are are consistent with growth from (qualitatively) hotter and/or drier melts, their trace element characteristics indicate that those melts were comparatively more evolved. In contrast, the dominant population of plagioclase crystals (both cores and rims) show higher Sr, Mg and lower Ba, Pb contents and are thus inferred to have crystallised from contrasting melts. On the basis of these characteristics we suggest that the high-An, low Sr (and Mg) plagioclase cores grew from melts with a significant (tens of percent) crustal component, although there is a diversity of possible crustal compositions available (Ewart and Stipp 1968; Charlier et al. 2010; Price et al. 2015). In contrast, the low Ba (and Pb) parts of the crystals are inferred to have grown from more broadly intermediate melts, with lower crustal

contributions. This inference is in line with evidence from the blue-grey cored Oruanui plagioclase crystals (Charlier et al. 2008), in which high An overgrowths around the cores were interpreted to have grown from almost 'pure' crustal melts with accompanying high $^{87}Sr/^{86}Sr$ values (see also Charlier et al. 2010). Such findings not only highlight the wide variety of source melt compositions and the open-system nature of the Oruanui reservoir, but also a heterogeneity of crustal sources and degrees of assimilation within different regions of the pre-eruptive mush body.

The role of mafic magma in the Oruanui eruption

In applications of the crystal mush model to the development of eruptible material, importance is often placed on the role that mafic magmas play in providing heat and volatiles to defrost and remobilise the mush (e.g. Bachmann and Bergantz 2006; Burgisser and Bergantz 2011; Huber et al. 2011; Karlstrom et al. 2012; Parmigiani et al. 2014; Bachmann and Huber 2016). Elevated rates of mafic intrusion have also been suggested as a mechanism for pre-eruptive heating and priming in post-Oruanui eruptions from Taupo (Barker et al. 2016). The involvement of two distinct, mafic magmas in the Oruanui eruption therefore raises questions as to what role these mafic magmas had in mush reactivation or initiating the eruption. The estimated total volume of mafic magma erupted (~3-5 km^3) is significantly larger than any other known eruption of purely mafic material in the TVZ (Wilson 2001). However, the ubiquitous down-temperature signatures in the rim-zones of the main crystal phases in the HSR (e.g. decreasing An in plagioclase, decreasing En in orthopyroxene) precludes the notion that injection of mafic material triggered the eruption through mafic recharge-driven heating (Fig. 5; cf. Barker et al. 2016). Wilson et al. (2006) suggested that some tholeiitic mafic magma may have ponded at the base of the primed Oruanui melt-dominant magma body in the weeks to months prior to eruption, and this is supported by evidence presented here for interaction between tholeiitic magma and the LSR and (but to a lesser extent) HSR magmas (Figs. 12 and 13). The resulting convection and stirring brought about by the hot mafic floor to the melt-dominant magma body was used by Wilson et al. (2006) to explain the homogenisation of any significant pre-existing compositional zonation. Here, we consider how such processes would be reflected in the zonation of minerals and in the textures in the mafic clasts.

Chemical analysis of the macroscopic crystals from individual mafic clasts (Figs. 8 and Fig. S.4) shows that many of these crystals are identical in composition to those found in

683 HSR and LSR clasts and hence inferred to be inherited. The positive Eu/Eu* values in almost
684 all of the tholeiitic clasts (Fig. 7) is also indicative that this magma has accumulated or
685 assimilated significant amounts of plagioclase. One of the two trends observed in the trace
686 element glass compositions of LSR plagioclase melt inclusions and selvedges (Fig. 2b) can
687 be explained by binary mixing between LSR compositions and the least-evolved tholeiitic
688 magma (Fig. 12). Trends within the mafic whole-rock data can be re-visited in the light of the
689 inference that the mafic magmas accumulated a significant component of 'rhyolitic' crystals.
690 Three similar, but subtly different trends are highlighted within the tholeiitic clasts (Fig. 13)
691 suggesting that the overall tholeiitic group itself may comprise at least three discrete batches
692 of magma. The overall patterns within the whole rock data trend towards LSR compositions,
693 with the exception of trend 3 on Fig. 13 (four samples) that plots on a compositional
694 trajectory towards HSR compositions. The whole-rock compositional trends within the mafic
695 magma suites, particularly the tholeiitic group, and the apparent mixing trend seen in the
696 glass data of LSR samples indicate that some mafic magma interacted with rhyolitic
697 compositions for an extended period before the clasts were quenched or the eruption
698 commenced.
699 In addition, a particular feature of the amphibole trace element data is the unusual
700 increase in Ni and Co abundance with decreasing Eu/Eu* and model crystallisation pressure
701 (Fig. 6c, d). These two elements occur at very low levels in the HSR rhyolite in general
702 (Table 2), although the MgO-enriched pumices reported by Wilson et al. (2006: see Table 1)
703 also have slightly enhanced levels of Ni and Co, barely discernible in their XRF data. Similar
704 results to those of Wilson et al. (2006) were reported by Kaneko et al. (2015), also from
705 whole-rock XRF data. Mafic recharge is unlikely, however, to have caused the increased Ni
706 and Co levels widely distributed in the amphiboles (i.e. those crystals from HSR pumices that
707 do not show higher MgO values) because the HSR amphiboles (plus orthopyroxene and
708 plagioclase) all are zoned outwards to compositions reflecting cooler and more evolved melt
709 compositions. We infer that the elevated amphibole Ni and Co levels reflect the dissolution of
710 a high Ni-Co phase into the HSR magma, with these elements then being sequestered into the
711 amphiboles. Of the other crystal phases in the Oruanui eruptives only the Fo_{85} olivines found
712 in the calc-alkaline mafic magmas are strongly enriched in these elements (Ni ~750 ppm; Co
713 ~180 ppm: Electronic Appendix 8). We infer that at some pre-eruptive stage(s), olivine-
714 bearing, relatively primitive mafic magma reached either the melt-dominant body or the
715 upper, evolved levels of the crystal mush zone and the olivines reacted out. Due to the
716 relatively low levels of other trace-elements in these olivines (see Electronic Appendix 8),

717 their dissolution into a large rhyolitic magma body would leave little trace, with Fe-Mg
718 contents being readily taken into ferromagnesian minerals in the rhyolitic assemblage or
719 slightly increasing the MgO content of a small fraction of the HSR. The elevated Ni and Co
720 contents in the HSR amphibole rims may thus be cryptic evidence for a role olivine-bearing
721 (i.e. calc-alkaline) mafic magma in the earlier assembly of the Oruanui melt-dominant
722 magma body than can be inferred from any other information at present.
723
724 **Diffusive timescales in the Oruanui magmatic system**
725 Elemental diffusion in volcanic crystals can be used to provide information about the
726 timescales of sub-surface processes (Costa et al. 2008, for review), and here we highlight
727 three mineral species in particular to place a range of temporal constraints on pre- and syn-
728 eruptive processes in the Oruanui magmatic system.
729
730 *Fe-Mg diffusion timescales in orthopyroxene*
731 Within the Oruanui magmas pre-eruptive timescales on the order of decades to millennia
732 have been obtained from modelling of Fe-Mg diffusion in orthopyroxenes. Allan et al. (2013)
733 modelled the prominent main core-rim boundaries in HSR orthopyroxenes (Fig. 3a), a feature
734 that they interpreted to represent the physical arrival of individual orthopyroxene crystals
735 along with their host LSR melt from the underlying mush into the growing melt-dominant
736 magma body. With allowance for maximum uncertainties in model parameters (especially
737 temperature and oxygen fugacity: Chamberlain et al. 2014a), it was inferred that the crystal-
738 liquid segregation process that led to the generation of the melt-dominant magma body did
739 not begin until only ~1600 years prior to the eruption, consistent with previous inferences
740 from zircon model-age spectra (Wilson and Charlier 2009). Probability density function
741 analysis indicated that the peak 'extraction age' was ~230 years earlier and that there was an
742 apparent period of stasis ~60 years just before the eruption.
743 With revisions to magmatic temperatures (Barker et al. 2015; this paper), and the
744 publication of a new model for Fe-Mg interdiffusion in magnesian olivine (Dohmen et al.
745 2016), we have revisited the timescale estimates of Allan et al. (2013). An extended
746 discussion is given in the supplementary material, but the various changes to parameters
747 (Table S.5), combined with the correction of a numerical error, leads to a reduction in
748 timescales of a factor of three (Fig. S.6). This migrates the peak extraction time to 80 years
749 pre-eruption with the inferred pre-eruption stasis period of 20 years (Figs. S.7 and S.8) but

750 does not substantively change the conclusion that mobilisation is geologically rapid, and by
751 implication involving the upwards transport of >1 km^3/y of magma). These timescales are
752 similar to those proposed from the faceting of Oruanui quartz-hosted melt inclusions
753 (Pamukcu et al. 2015), and both timescales may reflect the same process of rapid assembly of
754 the melt-dominant body, although the mineral species concerned come from different
755 domains within the mush.
756
757 *Fe-Ti diffusion timescales from magnetite*

758 BSE imagery of Fe-Ti oxide crystals extracted from the mafic clasts shows that many
759 magnetite crystals in these samples are compositionally zoned (Figs. 14 and S.9). Fe-Ti
760 oxides, and magnetite in particular, are known to rapidly re-equilibrate in response to
761 fluctuations in magmatic conditions (Freer and Hauptman 1978; Aragon et al. 1984;
762 Nakamura 1995; Venezky and Rutherford 1999; Coombs et al. 2000; Devine et al. 2003).
763 The preservation of Fe-Ti zonation in magnetites in the Oruanui mafic clasts, therefore, is
764 taken as a record of a process (or processes) operating shortly before quenching on eruption.
765 Using ImageJ (http://rsb.info.nih.gov.ij/), we retrieved spatially-resolved transects across the
766 BSE images and compared them to the chemical composition along the same transects as
767 measured by EPMA (e.g. Fig. 14). The greyscale values from the BSE images strongly
768 reflected changes in the Fe-Ti content of the magnetite. Although zonation in some minor
769 element oxides was also evident (e.g. Al_2O_3 and MgO), variations in the concentrations of
770 these elements appeared to have little or no influence over the greyscale zonation, allowing
771 the BSE intensity to be calibrated for Ti content. Using the changing greyscale intensity to
772 infer the changing Fe-Ti contents of the zoned crystals, we used the BSE images to recover
773 information about Fe-Ti zonation at a higher spatial resolution than that possible by direct
774 EPMA spot analyses. We modelled Fe-Ti interdiffusion in magnetite crystals to calculate the
775 timescale(s) over which mafic-felsic mingling occurred prior to quenching upon eruption
776 (Fig. 14). In order to determine the magnetite Fe-Ti diffusion coefficient in the Oruanui
777 system, we used the experimentally derived parameters of Aragon et al. (1984), and
778 conducted our modelling at conditions of 820 °C and an oxygen fugacity of NNO. These
779 conditions correspond to the lowest temperatures and oxygen fugacity conditions inferred
780 from the cores of equilibrium Fe-Ti oxide pairings within the mafic clasts (Fig. 11) and
781 should yield a maximum estimate. On this basis, the timescales obtained are between 6.7 and
782 37 hours (n = 18), but mostly <18 hours, and are interpreted to reflect syn-eruptive mixing

processes prior to quenching at the surface. Alternative modelling using diffusivity from Freer and Hauptmann (1978) at the same conditions of T and fO_2 yields timescales a factor of ~3 shorter than the Aragon et al. (1984) formulation, but this does not change the conclusion that the Fe-Ti oxide crystals record magma mixing processes occurring just hours before the magma was quenched. The samples used for modelling were from pumices in phase 7 ignimbrite, the coeval powerfully dispersed fall unit of which contains the greatest proportions of mafic material (up to 4 % of the juvenile fraction: Wilson 2001). Fall deposits of phases 6 and 7 are separated by a short time gap during which the eruption plume fully dissipated, but no erosion occurred (Wilson 2001). These factors suggest that the Fe-Ti oxide zonation reported here is recording syn-eruptive timescales related to inputs of fresh mafic magma during the time break between eruption phases 6 and 7.

Fe-Mg diffusion timescales from olivine

Despite the abundance of olivine in the calc-alkaline mafic clasts, very few crystals were suitable for Fe-Mg diffusion modelling. All of the large (1–2 mm) olivine crystals in the calc-alkaline samples have very thin (<5 μm) bright rims in the BSE images reflecting a higher Fe-content. However, closer inspection of the greyscale zonation patterns of the rims (which correlate directly to the changes in the Fe-Mg content of the olivine, e.g. Martin et al. 2008) suggests that these zonation features are not solely diffusion controlled, but reflect a quench crystallisation/growth feature of the olivines accompanying mafic-felsic interaction, indicated by regions of linear compositional gradient in the crystal rim and the lack of a single rim plateau value. Although the rim zonation was not suitable for more rigorous Fe-Mg diffusion modelling, examination of the interaction between the homogeneous cores and the growing rim zone does impart some constraints. Typically we see a very abrupt change between the core and the steadily increasing rim, with only a very narrow region of curvature between the two, which would be the natural consequence of diffusion. Based on the uniformly small length-scales of these regions (<5 μm), we can estimate a maximum timescale over which these regions of abrupt curvature could be preserved. Based on a temperature of ~820 °C and NNO oxygen fugacity, the olivine rim zonations are consistent with an event that occurred at most no more than a few weeks before quenching, consistent with short timescales inferred from experimental studies on olivine mixing with silicic melts (e.g. Coombs and Gardner 2004). Although more rigorous constraints are not available we suggest that it is possible that

the quench rims on the olivines formed during the same event recorded by the zoned magnetite crystals.

A cascade of events and their associated timescales as inferred from the Oruanui crystal archive

By combining our new results with previously published studies, an overview of the cascading timescales of pre- and syn-eruptive processes culminating in the Oruanui eruption is presented (Fig. 15). From these studies, it is clear that the overall history of the magmatic system that gave rise to the Oruanui eruption (and its precursory leaks: Sutton et al. 1995; Wilson and Charlier 2009) is not encapsulated in any one crystal phase or manifested on any one time scale.

At one extreme, the timescale for the growth of the Oruanui mush zone, with its distinctive chemical and isotopic compositional characteristics and zircon model-age spectra goes back around 40 kyr (Sutton et al. 1995; Wilson et al. 2006; Wilson and Charlier 2009). A model that used Oruanui zircon model-ages (Wilson and Charlier 2009) in isolation to infer a magma chamber lifetime of 200 kyr (Caricchi et al. 2014b) is flawed, for three reasons. First, the model-age spectrum used only represents those grains (or parts thereof) that yielded model ages 1 sd or more below the equiline in the U-Th disequilibrium system. The earliest ages presented in Wilson and Charlier (2009) are thus not indicative of the oldest ages present in the zircon suite. Second, a given age estimate from part of a zircon gives no indication in itself as to whether that age reflects material that is foreign and inherited through recycling (xenocrystic: cf. Charlier et al. 2005, 2010; Barker et al. 2014), consanguineous and inherited (antecrystic), or phenocrystic and growing in the magma body that actually erupted. There is thus no single zircon age determination (regardless of its precision) that can be uniquely defined as representing the onset of the Oruanui magmatic system. Third, during the ~200 kyr period prior to the Oruanui event, large volumes of volcanic products attest to the presence of compositionally unrelated magma systems (such as the NE dome system) active in the Taupo area (Sutton et al. 1995; Leonard et al. 2010; Cattell et al. 2016). The onset of the Oruanui magma system in terms of surface eruptives is around 60 ka (Sutton et al. 1995), and the commonality of a ~86-96 ka peak in zircon model ages for the Oruanui and earlier geochemically linked rhyolites (Charlier et al. 2005; Wilson and Charlier 2009) suggests a common source that experienced an enhanced episode of cooling and crystallisation at that time. The dominant younger peak of zircon model ages in

848 the Oruanui magma (37-41 ka across three samples: Wilson and Charlier 2009) also
849 represents a peak crystallisation in prior to formation of the Oruanui melt-dominant body at a
850 time when surface volcanism was inactive in the Taupo area (Wilson et al. 2009).
851 Extraction of melt plus entrained crystals to form the melt-dominant body only
852 occurred within the ~3000 year time gap between the Oruanui (25.4 ka) and its precursor
853 Okaia event at 28.6 ka from a geographically overlapping vent (Allan et al. 2013; Lowe et al.
854 2013) on the basis of the greatly contrasting zircon model-age spectra between the two suites
855 of products (Charlier et al. 2005; Wilson and Charlier 2009). This time gap is only bracketed
856 by the zircon data, but quantified in detail by the textural information and diffusion-profile
857 model age information from Oruanui pyroxenes to have been mostly accomplished in
858 decades to centuries (Allan et al. 2013; this paper). Faceting of quartz-hosted melt inclusions
859 (that were avoided in the work by Liu et al. 2006) also suggests a centennial timescale for the
860 lifetime of quartz growth in the melt-dominant body (Pamukcu et al. 2015).
861 Over years to days, interactions between the mafic and rhyolitic magmas are likely to
862 become important. In many examples globally it has been inferred that injection of mafic
863 magma into a body of evolved magma may precede eruption by days to months (e.g. Sparks
864 et al. 1977; Pallister et al. 1992; Snyder 2002; Leonard et al. 2002). In the case of the
865 Oruanui, however, evidence from the deposits of phases 1 and 2 also implies strongly that
866 external tectonic forces played a central role in starting and modulating the eruption during
867 these phases over comparable time periods (Allan et al. 2012). The evidence for the 'foreign'
868 NE-dome-type rhyolitic magma migrating at shallow levels into the Oruanui conduit again
869 implies strongly that the onset and initial stages of the eruption were not controlled by
870 properties (overpressure, volatile saturation, etc.) intrinsic to the magma chamber itself (cf.
871 Blake 1984; Foroozan et al. 2011; Gregg et al. 2012). What remains uncertain is whether the
872 large volumes of mafic magmas involved in the Oruanui eruption were opportunistic in
873 exploiting a changing stress field to rise into the mush zone and base of the melt-dominant
874 body, or whether the mafic magmas were active participants in controlling the crustal stress
875 field (Rowland et al. 2010). Evidence given above implies that some mafic magmas
876 interacted with the mush zone or the melt-dominant body prior to the eruption and that
877 multiple batches of magma were involved. However, these interactions were not to an extent
878 that led to any widespread heating signal in the compositions of crystals growing in the melt-
879 dominant body and thus were at best, minor. Later in the eruption sequence, diffusive time
880 estimates from Fe-Ti oxides suggest that the sharply defined onset of phase 7 coincided with
881 intra-eruptive injection of a batch of mafic magma. Such injections resulted in enhanced

882 juvenile mafic proportions, and may have also contributed to the marked escalations of
883 eruptive vigour into phases 3 (when LSR clasts also peak in abundance), 7 and 9 (Wilson
884 2001).
885 At the other extreme, the shortest timescales that can be quantified here are limited by
886 the ability of eruption products to preserve changing conditions in the crystal record. For the
887 Oruanui eruption, the limits are in those timescales that are captured by fast-diffusing
888 elements or species that can react to changes in physical conditions associated with magma
889 rise during eruptive activity. Water and CO_2 gradients in melt pockets in quartz (Liu et al.
890 2007) record rise rates of 5-35 cm/s as the magma started to actively vesiculate, and Li
891 gradients in quartz and feldspar record transient processes as the magma ascended at metres
892 to tens of metres per second (Charlier et al. 2012).
893
894 **Magmatism at Taupo: typical or unique for large silicic systems?**
895 Hildreth and Wilson (2007) put forward a model for the Bishop Tuff magma chamber in
896 which gradients in melt chemistry, crystal content and temperature were established and
897 maintained through incremental accumulation from a source mush reservoir. Subsequent
898 work on mineral-specific aspects of the Bishop record has reinforced that concept
899 (Chamberlain et al. 2015; Evans et al. 2016). This model is broadly similar to that for the
900 Oruanui proposed by Allan et al. (2013) and re-emphasised here. However, several features
901 of the two deposits are in stark contrast to one another. For example, the Bishop Tuff magma
902 was compositionally zoned at the time of eruption such that first erupted compositions were
903 the most evolved, while less-evolved and more crystal-rich compositions became more
904 prominent as the eruption progressed (Hildreth 1979; Hildreth and Wilson 2007). There thus
905 cannot have been significant large-scale convection operating in the Bishop magma chamber.
906 In contrast, the Oruanui magma, although compositionally diverse, was not zoned in any
907 systematic way (Fig. S.1). This feature and the diversity of mineral and melt inclusion
908 compositions and textures in any one clast (Liu et al. 2006; Wilson et al. 2006, 2012; Wilson
909 and Charlier 2009; this paper) imply that the Oruanui magma body was vigorously
910 convecting.
911 Early-erupted crystals in the Bishop magma lack prominent zonation and lack
912 evidence for any significant and widespread dissolution/disequilibrium features (Hildreth
913 1979; Chamberlain et al. 2015), leading Hildreth (1979) to conclude that the Bishop Tuff
914 magma underwent largely *in situ* crystallisation and that the crystal cargo was phenocrystic

915 (in the sense used in this paper). Later-erupted Bishop crystals do, however, show evidence
916 for influx of a contrasting magma, growth of compositionally contrasting rims on quartz,
917 feldspar and zircons, and introduction of pyroxenes (Peppard et al. 2001; Wark et al. 2007;
918 Reid et al. 2011; Gualda et al. 2012a; Chamberlain et al. 2014a,b, 2015; Gualda and Sutton
919 2016). Oruanui HSR crystals often have two, readily identifiable and distinct periods of
920 growth. In the orthopyroxene and plagioclase, the earlier and later histories are readily
921 distinguished on the basis of resorption horizons ± sieved texturing or patchy zonation in the
922 cores (Fig. 3), features which are absent in the crystals of the Bishop Tuff. The earlier
923 growth stage is inferred to have occurred within the thermally and compositionally zoned
924 mush body, and the other is reflected in the rim-zones crystallised within the melt-dominant
925 magma body. This melt-dominant body, stirred by convective mixing, also evolved over time
926 (decades), as seen in the decreases in An proportions in plagioclase rims to An_{38} and En in
927 the orthopyroxene rims to En_{46}.
928 The question then arises, that if both magma bodies accumulated following broadly
929 similar mechanisms, what factors led to the strongly contrasting characteristics of the melt-
930 dominant magma bodies and their crystal cargoes? We suggest that the answer lies in the
931 process(es) that ultimately drive the crystal-liquid segregation and the rates at which large-
932 scale melt extraction process take place. In the Oruanui, physical extraction from the mush
933 and assembly of the melt-dominant magma body was extremely rapid, at rates exceeding >1
934 km^3/y (Wilson and Charlier 2009; Allan et al. 2013; this paper). Similarly rapid rates of melt
935 extraction have also been demonstrated to have occurred prior to younger eruptions from
936 Taupo (Barker et al. 2016). Allan et al. (2013) suggested that magma-assisted rifting
937 processes prior to the Oruanui eruption may have acted to enhance the melt extraction
938 process by creating gashes through the mush body that acted as focussing channels for melt
939 (and crystals) to migrate upwards and accumulate, as compared with more passive processes
940 (e.g. hindered settling, gas filter pressing) that are generally assumed to drive melt extraction
941 (Bachmann and Huber 2016 for overview). The vigour with which melt and crystals from
942 contrasting compositions, depths and temperatures were brought together in the shallow
943 crustal holding chamber, and the inferred heat loss associated with the 40-50 °C cooling
944 (Allan et al. 2013; this paper), likely resulted in convection and stirring that acted to destroy
945 any chamber-wide compositional and thermal gradients during formation of the melt-
946 dominant magma body. Any early increments of mafic magma that reached the floor of the
947 melt-dominant body may also have served to intensify the mixing processes through
948 providing a source of heat and volatiles (e.g. Sparks et al. 1984). However, such increments

949 were not big enough in volume to counteract the overall cooling of the melt-dominant HSR
950 body, as reflected in the ubiquitous down-temperature signals in compositions of the major
951 crystal phases.
952 In contrast, no mineral textures that could represent the contrasts between growth in
953 the crystal-dominant mush versus that in the melt-dominant body above have been clearly
954 identified in the Bishop eruption products (particularly the early-erupted material). A
955 maximum timescale for accumulation of the Bishop melt-dominant body has been suggested
956 as 70-80 kyr based on zircon textural and age relationships (Chamberlain et al. 2014b). Much
957 shorter timescales proposed from diffusive profiling across zonation boundaries in quartz
958 (Gualda et al. 2012a; Gualda and Sutton 2016) and melt inclusion faceting (Pamucku et al.
959 2015) are interpreted to reflect only the later stages of mixing events that gave rise to zoned
960 crystals (quartz, sanidine, zircon) in the later-erupted, deeper-derived parts of the melt-
961 dominant body (Chamberlain et al. 2014a, 2015). It seems necessary that in order to maintain
962 the apparent equilibrium relationships between crystals and melt, and the vertical
963 compositional and thermal stratification, the fluid dynamical processes involved in the melt-
964 dominant magma bodies must have been much more sluggish in the Bishop than the Oruanui.
965 Identifying minerals, or portions thereof, as phenocrystic, antecrystic or xenocrystic in
966 the Oruanui pumices is challenging. The clearest xenocrystic components are older zircons
967 found as whole grains or cores, and identifiable as such from their age spectra (Charlier et al.
968 2005, 2010), quartz cores with contrasting entrapped melt inclusion compositions (Liu et al.
969 2006) and cloudy feldspar cores with contrasting Sr-isotopic systematics (Charlier et al.
970 2008). The sieve-textured or resorbed cores in the Oruanui HSR plagioclase and
971 orthopyroxenes (Fig. 3) could be characterised as antecrystic, with the interiors having grown
972 in a parental, mush-like reservoir that was, however, physically, compositionally and
973 temporally distinct from the melt-dominant magma body that ultimately erupted. The zircons
974 defining the ~95 ka and 41-37 ka model-age peaks in the Oruanui and its precursor eruptions
975 are also antecrystic on this basis. The phenocryst population, *sensu stricto*, present in the
976 Oruanui pumices is thus quite restricted. It includes the rim-zones of those crystals (quartz,
977 feldspar, orthopyroxene) that have resorbed or non-equilibrium cores, together with the
978 sparse grains of the same minerals that have homogeneous textures and compositions
979 appropriate to the melt-dominant body (e.g. crystallisation model temperatures diminishing
980 from ~840 to ~790 °C). The Fe-Ti oxides are phenocrystic, regardless of their antecedents,
981 because any inheritance patterns are erased by rapid diffusion. The Fe-Ti oxides therefore
982 remained in equilibrium with conditions in the melt-dominant body (and the rim

compositions of other crystal phases) for all except the shortest timescales (hours to days) associated with syn-eruptive magma mixing (Fig. 14). Amphiboles include antecrystic cores and phenocrystic rims (plus subordinate phenocrystic grains), but these are only identifiable by chemical analysis, particularly of trace elements (Figs. 6 and S.5), and are not distinguishable on a textural basis. The bulk crystal population in the Oruanui system is thus not amenable to equilibrium modelling (cf. Bégué et al. 2014) as the majority of the crystal mass is inherited and the host melt temperature decreasing rapidly, with corresponding changes in the outwards crystallising compositions.

Wilson et al. (2006) presented a scaled, schematic cross section of the Oruanui magmatic system immediately prior to eruption. This cross section is revised and updated here in Fig. 16 in light of new details from Allan et al. (2012, 2013) and the findings of this study. Integration of the existing information and new datasets presented here highlight the following details:

1) The realisation that tectonic rifting-related processes played an integral part in triggering the onset of the Oruanui eruption. A body of biotite-bearing rhyolite magma was present in the shallow crust beneath the NE dome system (Figs. 1 and 16: Sutton et al. 1995; Wilson and Charlier 2009). Syn-eruptive rifting processes resulted in the southerly propagation of NE-dome-type rhyolite magma laterally, to intercept Oruanui HSR magma in the conduit during phases 1 and 2 of the eruption (Allan et al. 2012). Comparable tectonic controls may well have been important in other large, caldera-forming events (e.g. Myers et al. 2016), but the evidence more subtle and not involving magmas of obviously contrasting visible or compositional characteristics.

2) The approximate depth to the top of the melt-dominant magma body. Although similar to that proposed from volatile data (Liu et al. 2006), newer data suggest that its top may have been slightly shallower and lay between ~3.5 and 6.0 km depth (~90 to 140 MPa). These dimensions, inferred from thermobarometry applied to the outermost rims of amphibole crystals in the HSR, are consistent with the lack of thermal and compositional gradient within the body, and consistent with it being contained within Wilson's (2001) areas 'A' (the structural caldera collapse area) and 'B' (the collapse collar: terms after Lipman 1997) of the Oruanui caldera (Fig. 1).

3) Recognition of the crystal diversity and a range of potential source regions. Approximately 90% of the crystal cargo in the HSR is inferred to have cores and interior domains that were inherited from a stratified crystal mush body prior to their confluence in the melt-dominant magma body. Quartz crystals are inferred to have originated from an

upper, cooler, SiO_2-saturated and highly-evolved layer, whereas the majority of amphibole, orthopyroxene and plagioclase crystals largely originated from deeper, lesser-evolved levels.

4) Origin of the LSR pumices. The LSR pumices were originally inferred by Wilson et al. (2006) to represent deeper and hotter parts of the melt dominant body. Here, these samples (as represented by individual pumices) are now interpreted to represent isolated bodies of crystal-poor rhyolite that were held within the crystal mush and were tapped syn-eruptively (e.g. Cashman and Giordano 2014). In addition, the LSR melt (and entrained crystals) is recognised by us as having also previously been the feedstock material for the melt-dominant body. These conclusions are based on the distinct differences between the HSR and LSR glass chemistries (Fig. 2) and limited degrees of hybridisation in the pumices (i.e. minor melt and crystal exchanges between HSR and LSR, as inferred by Allan et al. 2013).

4) Wilson et al. (2006) suggested that the Oruanui mafic magmas, in particular the tholeiitic magma, had ponded at the base of the melt-dominant magma body and initiated chamber wide stirring and homogenisation. Subsequent work (Allan et al. 2013; Rooyakkers 2015; this paper) has shown that the mafic magmas were mostly interacting with the mush, as indicated by their accumulated felsic crystal populations and whole-rock trajectories trending towards LSR (rather than HSR) compositions (Figs. 12 and 13). Commensurate with this revised interpretation, our data imply that vigorous convection was an inherent feature of the melt-dominant body from the moment of its inception, and not simply the result of late-stage introduction of mafic magmas.

Conclusions

The assembly and eruption of the Oruanui magma body was a complex, but geologically short-lived, sequence of events. The work presented here and in other papers cited shows that there is a rich petrological record of these events in the compositions of melts and minerals, and in the textures of the mineral phases. The associated processes can be resolved into a cascade of events over timescales ranging from tens of thousands of years for the development of the deeper source mush zone to hundreds of seconds for the latest stages of magma rise before fragmentation and quenching. Key conclusions from the integration of previous and current Oruanui datasets are as follows.

1. Detailed compositional and textural records within Oruanui HSR quartz, plagioclase, orthopyroxene and amphibole crystals highlight the transition from

1050 compositional diversity in their early histories, to uniformity immediately prior to eruption.
1051 Melt extraction from the mush zone entrained crystals from all levels of the stratified crystal
1052 mush body, resulting in the juxtaposition of a diverse range of crystals within the melt-
1053 dominant magma body. A general outwards-cooling trend reflected in most mineral
1054 compositions show that the melt-dominant body cooled by ~40-50 ºC during its lifetime and
1055 at that rate would have cooled back to mush within a few centuries to millenia had evacuation
1056 not occurred. Our data support the concept that eruptible magma bodies are very short-lived
1057 when compared to the overall lifetime of the parental magmatic system (e.g. Glazner et al.
1058 2004; Barboni and Schoene 2014; Barker et al. 2016).
1059 2. The Oruanui mafic magmas record significant interactions with, or inheritance of,
1060 'rhyolite' crystals (i.e. crystals with compositions appropriate for growth from rhyolite melts)
1061 from traversing through the mush zone during their eruption. Inheritance occurred over
1062 varying timescales, with reaction rims varying from only a few microns to >100 μm.
1063 However, ubiquitous down-temperature signals recorded in HSR crystals precludes the
1064 possibility that mafic magmas played any significant role in wholesale re-heating and/or re-
1065 mobilisation of the mush to cause eruption (cf. Bachmann and Dungan 2002; Huber et al.
1066 2011; Barker et al. 2016). Syn-eruptive interactions between the mafic magmas and the melt-
1067 dominant magma body are recorded in zoned magnetite and olivine crystals, down to
1068 timescales of hours to tens of hours. Such short-term interactions can be directly linked with
1069 inferred eruptive timings and variations in the erupted proportions of mafic materials (Wilson
1070 2001).
1071 3. The disparate textural and compositional domains within single crystals,
1072 particularly HSR plagioclase and orthopyroxene, make complex the definitions of
1073 phenocrysts versus antecrysts for the Oruanui system. Despite the near-uniformity of rim
1074 compositions in the HSR crystals, the compositions and intensive parameters recorded by the
1075 crystal cores and interiors bear no direct relation to the melt-dominant body in which they
1076 were immersed at the time of eruption.
1077 4. The magmatic systems giving rise to voluminous, crystal-poor rhyolites can be
1078 considered to operate in general on two contrasting timescales: longer-term processes
1079 governing the broad compositional characteristics of the magma (i.e. fractional
1080 crystallisation, protolith assimilation, etc.) versus short-lived processes governing physical
1081 assembly of the melt dominant magma body that actually erupts. The major crystallisation
1082 associated with the Oruanui magmatic system is represented by a dominant peak of zircon
1083 model ages centred on ~37-41 ka (Charlier et al. 2005; Wilson and Charlier 2009), in accord

with the U/Th model age of bulk separates of the main crystal phases of 33 ka (+18 ka/– 16 ka: Charlier et al. 2005). Physical assembly of the melt-dominant magma body, as reflected in orthopyroxene zoning (Allan et al. 2013; this paper) and melt inclusion faceting (Pamukcu et al. 2015), occurred in <600 years, and mainly within the last ~100 years prior to eruption (i.e. 2-3 orders of magnitude faster than the processes of chemical evolution in the progenitor melts). On a global scale, such accumulation rates for eruptible magma are at the extreme, especially for such a large-sized eruption and appear to reflect the influence of tectonic processes acting on a mush system that held large quantities of melt. Only slightly smaller rates applied also to the youngest eruptions at Taupo (Barker et al. 2016). Both rate estimates are apparently orders of magnitude faster than those inferred for the comparably-sized Bishop Tuff system (Chamberlain et al. 2014b; Simon et al. 2014).

5. The model inferred for the Oruanui magma system (extraction of melt plus some fraction of crystals from a crystal mush into a melt-dominant holding chamber) is similar to the model invoked for the Bishop Tuff (Hildreth and Wilson 2007; Chamberlain et al. 2015). Despite these broad similarities, the zonation characteristics of the deposits from these two eruptions are greatly different at whole-rock and single-crystal scales, reflecting different accumulation timescales for the respective melt-dominant bodies. The rapidity with which the Oruanui melt-dominant magma body accumulated, and the inferred rapid rates of heat loss, led to vigorous convection that destroyed any significant compositional and thermal zonation within the melt-dominant magma body prior to eruption.

6. The timescales inferred either for the lifetime of the overall Oruanui magmatic system or accumulation of its ~530 km^3 melt-dominant magma body are much shorter than generalised estimates based on numerical modelling for similar sized magma bodies (e.g. Bachmann and Bergantz 2004; Annen 2009; Gelman et al. 2013; Caricchi et al 2014b). The involvement of the mafic magmas, and the rapid accumulation of the melt-dominant magma body is inferred to be the consequence of an enhanced episode of (magma-assisted) rifting in the crystal mush-bearing crust beneath Taupo during the lead-in to the Oruanui eruption. Following Rowland et al. (2010) we infer that tectonism associated with the rifted arc setting served to be a major (dominant?) control on (a) the rapidity of accumulation of the Oruanui melt-dominant body, (b) the fact that it grew to such a large size without prematurely evacuating, and (c) its consequent release on eruption in spasmodic fashion. Such a strong control by a non-volcanic factor raises questions as to how tectonic processes might have acted to control the development and eruption of other large caldera-related silicic systems.

Acknowledgements

This work was supported by the Marsden Fund administered by the Royal Society of New Zealand (Grant VUW0813 to CJNW), a Bright Futures Top Achiever Doctoral Scholarship (for ASRA) administered by the Tertiary Education Commission of New Zealand, and Victoria University scholarships for SJB (PhD) and SMR (MSc). CJNW also acknowledges award of a James Cook Fellowship, administered by the Royal Society of New Zealand. We thank John Gamble, Jim Cole and Steve Blake for illuminating comments and discussions, and an anonymous reviewer, Michelle Coombs and, especially, Laura Waters for their comments.

References

Allan ASR, Baker JA, Carter L, Wysoczanski RJ (2008) Reconstructing the Quaternary evolution of the world's most active silicic volcanic system: insights from an ~1.65 Ma deep ocean tephra record sourced from Taupo Volcanic Zone, New Zealand. Quat Sci Rev 27:2341-2360

Allan ASR, Wilson CJN, Millet M-A, Wysoczanski RJ (2012) The invisible hand: tectonic triggering and modulation of a rhyolitic supereruption. Geology 40:563-566

Allan ASR, Morgan DJ, Wilson CJN, Millet M-A (2013) From mush to eruption in centuries: assembly of the super-sized Oruanui magma body. Contrib Mineral Petrol 166:143-164

Annen C (2009) From plutons to magma chambers: thermal constraints on the accumulation of eruptible silicic magma in the upper crust. Earth Planet Sci Lett 284:409-416

Aragon R, McCallister RH, Harrison HR (1984) Cation diffusion in titanomagnetites. Contrib Mineral Petrol 85:174-185

Bachmann O, Bergantz GW (2004) On the origin of crystal-poor rhyolites: extracted from batholithic crystal mushes. J Petrol 45:1565-1582

Bachmann O, Bergantz GW (2006) Gas percolation in upper-crustal silicic crystal mushes as a mechanism for upward heat advection and rejuvenation of near-solidus magma bodies. J Volcanol Geotherm Res 149:85-102

Bachmann O, Bergantz GW (2008) Rhyolites and their source mushes across tectonic settings. J Petrol 49:2277-2285

Bachmann O, Dungan MA (2002) Temperature-induced Al-zoning in hornblendes of the Fish Canyon magma, Colorado. Am Mineral 87:1062-1076

Bachmann O, Huber C (2016) Silicic magma reservoirs in the Earth's crust. Am Mineral 101:2377-2404

Bacon CR, Hirschmann MM (1988) Mg/Mn partitioning as a test for equilibrium between coexisting Fe-Ti oxides. Am Mineral 73:57-61

Bacon CR, Lowenstern JB (2005) Late Pleistocene granodiorite source for recycled zircon and phenocrysts in rhyodacite lava at Crater Lake, Oregon. Earth Planet Sci Lett 233:277-293

Bain AA, Jellinek AM, Wiebe RA (2013) Quantitative field constraints on the dynamics of silicic magma chamber rejuvenation and overturn. Contrib Mineral Petrol 165:1275-1294

Barboni M, Schoene B (2014) Short eruption window revealed by absolute crystal growth rates in a granitic magma. Nature Geosci 7:524-528

Barker SJ, Wilson CJN, Smith EGC, Charlier BLA, Wooden J, Hiess J, Ireland TR (2014) Post-supereruption magmatic reconstruction of Taupo volcano (New Zealand), as reflected in zircon ages and trace elements. J Petrol 55:1511-1533

Barker SJ, Wilson CJN, Allan ASR, Schipper CI (2015) Fine-scale temporal recovery, reconstruction and evolution of a post-supereruption magmatic system: Taupo (New Zealand). Contrib Mineral Petrol 170:5

Barker SJ, Wilson CJN, Morgan DJ, Rowland JV (2016) Rapid priming, accumulation and recharge of magma driving recent eruptions at a hyperactive caldera volcano. Geology 44:323-326

Bégué F, Gualda GAR, Ghiorso MS, Pamukcu AS, Kennedy BM, Gravley DM, Deering CD, Chambefort I (2014) Phase-equilibrium geobarometers for silicic rocks based on rhyolite-MELTS. Part 2: application to Taupo Volcanic Zone rhyolites. Contrib Mineral Petrol 168:1082

Bégué F, Gravley DM, Chambefort I, Deering CD, Kennedy BM (2015) Magmatic volatile distribution as recorded by rhyolitic melt inclusions in the Taupo Volcanic Zone, New Zealand. In: Zellmer GF, Edmonds M, Straub SM (eds) The role of volatiles in the genesis, evolution and eruption of arc magmas. Geol Soc Lond Spec Pub 410:71-94

Blake S (1984) Volatile oversaturation during the evolution of silicic magma chambers as an eruption trigger. J Geophys Res 89:8237-8244

Brey GP, Kohler T (1990) Geothermobarometry in 4-phase lherzolites 2. New thermobarometers, and practical assessment of existing thermobarometers. J Petrol 31:1353-1378

1184 Brophy JG (1991) Compositional gaps, critical crystallinity, and fractional crystallization in
1185 orogenic (calc-alkaline) magmatic systems. Contrib Mineral Petrol 109:173-182
1186 Brown SJA, Wilson CJN, Cole JW, Wooden J (1998) The Whakamaru group ignimbrites,
1187 Taupo Volcanic Zone, New Zealand: evidence for reverse tapping of a zoned silicic
1188 magma system. J Volcanol Geotherm Res 84:1-37
1189 Burgisser A, Bergantz GW (2011) A rapid mechanism to remobilize and homogenize highly
1190 crystalline magma bodies. Nature 471:212-217
1191 Caricchi L, Annen C, Blundy J, Simpson G, Pinel V (2014a) Frequency and magnitude of
1192 volcanic eruptions controlled by magma injection and buoyancy. Nature Geosci 7:126-
1193 130
1194 Caricchi L, Simpson G, Schaltegger U (2014b) Zircons reveal magma fluxes in the Earth's
1195 crust. Nature 511:457-461
1196 Cashman KV, Giordano G (2014) Calderas and magma reservoirs. J Volcanol Geotherm Res
1197 288:28-45
1198 Cattell HJ, Cole JW, Oze C (2016) Volcanic and sedimentary facies of the Huka Group arc-
1199 basin sequence, Wairakei–Tauhara Geothermal Field, New Zealand. NZ J Geol
1200 Geophys 59:236-256
1201 Chamberlain KJ, Morgan DJ, Wilson CJN (2014a) Timescales of mixing and mobilisation in
1202 the Bishop Tuff magma body: perspectives from diffusion chronometry. Contrib
1203 Mineral Petrol 168:1034
1204 Chamberlain KJ, Wilson CJN, Wooden JL, Charlier BLA, Ireland TR (2014b) New
1205 perspectives on the Bishop Tuff from zircon textures, ages and trace elements. J Petrol
1206 55:395-426
1207 Chamberlain KJ, Wilson CJN, Wallace PJ, Millet M-A (2015) Micro-analytical perspectives
1208 on the Bishop Tuff magma chamber. J Petrol 56:605-640
1209 Charlier BLA, Wilson CJN, Lowenstern JB, Blake S, van Calsteren PW, Davidson JP (2005)
1210 Magma generation at a large, hyperactive silicic volcano (Taupo, New Zealand)
1211 revealed by U–Th and U–Pb systematics in zircons. J Petrol 46:3-32
1212 Charlier BLA, Wilson CJN, Davidson JP (2008) Rapid open-system assembly of a large
1213 silicic magma body: time-resolved evidence from cored plagioclase crystals in the
1214 Oruanui eruption deposits, New Zealand. Contrib Mineral Petrol 156:799-813
1215 Charlier BLA, Wilson CJN, Mortimer N (2010) Evidence from zircon U-Pb age spectra for
1216 crustal structure and felsic magma genesis at Taupo volcano, New Zealand. Geology
1217 38:915-918

1218 Charlier BLA, Morgan DJ, Wilson CJN, Wooden JL, Allan ASR, Baker JA (2012) Lithium
1219 concentration gradients in feldspar and quartz record the final minutes of magma ascent
1220 in an explosive supereruption. Earth Planet Sci Lett 319-320:218-227
1221 Coombs ML, Gardner JE (2004) Reaction rim growth on olivine in silicic melts: implications
1222 for magma mixing. Am Mineral 89:748-759
1223 Coombs ML, Eichelberger JC, Rutherford MJ (2000) Magma storage and mixing conditions
1224 for the 1953-1974 eruptions of Southwest Trident volcano, Katmai National Park,
1225 Alaska. Contrib Mineral Petrol 140:99-118
1226 Costa F, Dohmen R, Chakraborty S (2008) Timescales of magmatic processes from
1227 modelling the zoning patterns of crystals. In: Putirka KD, Tepley FJ (eds) Minerals,
1228 inclusions and volcanic processes. Rev Mineral Geochem 69:545-594
1229 Davidson JP, Hora JM, Garrison JM, Dungan MA (2005) Crustal forensics in arc magmas. J
1230 Volcanol Geotherm Res 140:157-170
1231 de Silva SL, Gregg PM (2014) Thermomechanical feedbacks in magmatic systems:
1232 implications for growth, longevity, and evolution of large caldera-forming magma
1233 reservoirs and their supereruptions. J Volcanol Geotherm Res 282:77-91
1234 Devine JD, Rutherford MJ, Norton GE, Young SR (2003) Magma storage region processes
1235 inferred from geochemistry of Fe-Ti oxides in andesitic magma, Soufrière Hills
1236 Volcano, Montserrat, WI. J Petrol 44:1375-1400
1237 Dohmen R, Ter Heege JH, Becker H-W, Chakraborty S (2016) Fe-Mg interdiffusion in
1238 orthopyroxene. Am Mineral (in press) doi:10.2138/am-2016-5815
1239 Dungan MA, Davidson J (2004) Partial assimilative recycling of the mafic plutonic roots of
1240 arc volcanoes: an example from the Chilean Andes. Geology 32:773-776
1241 Eichelberger JC (1978) Andesitic volcanism and crustal evolution. Nature 275:21-27
1242 Evans BW, Bachmann O (2013) Implications of equilibrium and disequilibrium among
1243 crystal phases in the Bishop Tuff. Am Mineral 98:271-274
1244 Evans BW, Hildreth W, Bachmann O, Scaillet B (2016) In defence of magnetite-ilmenite
1245 thermometry in the Bishop Tuff and its implication for gradients in silicic magma
1246 reservoirs. Am Mineral 101:469-482
1247 Evans BW, Scaillet B, Keuhner SK (2006) Experimental determination of coexisting iron–
1248 titanium oxides in the systems FeTiAlO, FeTiAlMgO, FeTiAlMnO, and
1249 FeTiAlMgMnO at 800 and 900 °C, 1–4 kbar, and relatively high oxygen fugacity.
1250 Contrib Mineral Petrol 152:149-167

1251 Ewart A, Stipp JJ (1968) Petrogenesis of the volcanic rocks of the central North Island, New
1252 Zealand, as indicated by a study of Sr^{87}/Sr^{86} ratios, and Sr, Rb, K, U and Th
1253 abundances. Geochim Cosmochim Acta 32:699-736
1254 Foroozan R, Elsworth D, Voight B, Mattioli GS (2011) Magmatic-metering controls the
1255 stopping and restarting of eruptions. Geophys Res Lett 38:L05306
1256 Freer R, Hauptman Z (1978) Experimental study of magnetite-titanomagnetite interdiffusion.
1257 Phys Earth Planet Int 16:223-231
1258 Gamble JA, Wood CP, Price RC, Smith IEM, Stewart RB, Waight T (1999) A fifty year
1259 perspective of magmatic evolution on Ruapehu Volcano, New Zealand: verification of
1260 open system behaviour in an arc volcano. Earth Planet Sci Lett 170:301-314
1261 Gelman SE, Gutierrez FJ, Bachmann O (2013) On the longevity of large upper crustal silicic
1262 magma reservoirs. Geology 41:759-762
1263 Ghiorso MS, Evans BW (2008) Thermodynamics of rhombohedral oxide solid solutions and
1264 a revision of the Fe-Ti two-oxide geothermometer and oxygen-barometer. Am J Sci
1265 308:957-1039
1266 Girard G, Stix J (2010) Rapid extraction of discrete magma batches from a large
1267 differentiating magma chamber: the Central Plateau Member rhyolites, Yellowstone
1268 caldera, Wyoming. Contrib Mineral Petrol 160:441-465
1269 Glazner AF, Bartley JM, Coleman DS, Gray W, Taylor RZ (2004) Are plutons assembled
1270 over millions of years by amalgamation from small magma chambers? GSA Today
1271 14(4/5):4-11
1272 Gregg PM, de Silva SL, Grosfils EB, Parmigiani JP (2012) Catastrophic caldera-forming
1273 eruptions: thermomechanics and implications for eruption triggering and maximum
1274 caldera dimensions on Earth. J Volcanol Geotherm Res 241-242:1-12
1275 Gualda GAR, Sutton SR (2016) The year leading to a supereruption. PLoS ONE
1276 11:e0159200
1277 Gualda GAR, Pamukcu AS, Ghiorso MS, Anderson AT, Sutton SR, Rivers ML (2012a)
1278 Timescales of quartz crystallization and the longevity of the Bishop giant magma body.
1279 PLoS ONE 7:e37492
1280 Gualda GAR, Ghiorso MS, Lemons RV, Carley TL (2012b) Rhyolite-MELTS: a modified
1281 calibration of MELTS optimized for silica-rich, fluid-bearing magmatic systems. J
1282 Petrol 53:875-890
1283 Hammond PA, Taylor LA (1982) The ilmenite/titano-magnetite assemblage: kinetics of re-
1284 equilibration. Earth Planet Sci Lett 61:143-150

1285 Hellstrom J, Paton C, Woodhead JD, Hergt JM (2008) Iolite: software for spatially resolved
1286 LA-(quad and MC) ICPMS analysis. In: Sylvester, P (ed) Laser Ablation ICP-MS in
1287 the Earth Sciences: Current Practices and Outstanding Issues. Mineral Assoc Can Short
1288 Course Ser 40:343-348
1289 Hildreth W (1979) The Bishop Tuff: evidence for the origin of compositional zonation in
1290 silicic magma chambers. In: Chapin CE, Elston WE (eds) Ash-flow Tuffs. Geol Soc
1291 Am Spec Pap 180:43-75
1292 Hildreth W (2004) Volcanological perspectives on Long Valley, Mammoth Mountain, and
1293 Mono Craters: several contiguous but discrete systems. J Volcanol Geotherm Res
1294 136:169-198
1295 Hildreth W, Wilson CJN (2007) Compositional zoning of the Bishop Tuff. J Petrol 48:951-
1296 999
1297 Housh TB, Luhr JF (1991) Plagioclase-melt equilibria in hydrous systems. Am Mineral
1298 76:477-492
1299 Huang R, Audétat A (2012) The titanium-in-quartz (TitaniQ) thermobarometer: a critical
1300 examination and re-calibration. Geochim Cosmochim Acta 84:75-89
1301 Huber C, Bachmann O, Manga M (2010) Two competing effects of volatiles on heat transfer
1302 in crystal-rich magmas: thermal insulation vs defrosting. J Petrol 51:847-867
1303 Huber C, Bachmann O, Dufek J (2011) Thermo-mechanical reactivation of locked crystal
1304 mushes: melting-induced internal fracturing and assimilation processes in magmas.
1305 Earth Planet Sci Lett 304:443-454
1306 Huber C, Bachmann O, Dufek J (2012) Crystal-poor versus crystal-rich ignimbrites: a
1307 competition between stirring and reactivation. Geology 40:115-118
1308 Jellinek AM, DePaolo DJ (2003) A model for the origin of large silicic magma chambers:
1309 precursors of caldera-forming eruptions. Bull Volcanol 65:363-381
1310 Kaneko K, Inoue K, Koyaguchi T, Yoshikawa M, Shibata T, Takahashi T, Furukawa K
1311 (2015) Magma plumbing system of the Aso-3 large pyroclastic eruption cycle at Aso
1312 volcano, Southwest Japan: petrological constraint on the formation of a compositionally
1313 stratified magma chamber. J Volcanol Geotherm Res 303:41-58
1314 Karlstrom L, Rudolph ML, Manga M (2012) Caldera size modulated by the yield stress
1315 within a crystal-rich magma reservoir. Nature Geosci 5:402-405
1316 Langridge RM, Ries W, Litchfield NJ, Villamor P, Van Dissen RJ, Barrell DJA, Rattenbury
1317 MS, Heron DW, Haubrock S, Townsend DB, Lee JM, Berryman KR, Nicol A, Cox SC,

1318 Stirling MW (2016) The New Zealand active faults database. NZ J Geol Geophys
1319 59:86-96
1320 Leonard GS, Cole JW, Nairn IA, Self S (2002) Basalt triggering of the c. AD 1305 Kaharoa
1321 rhyolite eruption, Tarawera Volcanic Complex, New Zealand. J Volcanol Geotherm
1322 Res 115:461-486
1323 Leonard GS, Begg JG, Wilson CJN (2010) Geology of the Rotorua area. Institute of
1324 Geological and Nuclear Sciences 1:250,000 geological map 5. Lower Hutt: Institute of
1325 Geological & Nuclear Sciences
1326 Lipman PW (1997) Subsidence of ash-flow calderas: relation to caldera size and magma-
1327 chamber geometry. Bull Volcanol 59:198-218
1328 Liu Y, Anderson AT, Wilson CJN, Davis AM, Steele IM (2006) Mixing and differentiation
1329 in the Oruanui rhyolitic magma, Taupo, New Zealand: evidence from volatiles and
1330 trace elements in melt inclusions. Contrib Mineral Petrol 151:71-87
1331 Liu Y, Anderson AT, Wilson CJN (2007) Melt pockets in phenocrysts and ascent rates of
1332 silicic magmas. J Geophys Res 112:B06204
1333 Lowe DJ, Shane PAR, Alloway BV, Newnham RM (2008) Fingerprints and age models for
1334 widespread New Zealand tephra marker beds erupted since 30,000 years ago: a
1335 framework for NZ-INTIMATE. Quat Sci Rev 27:95-126
1336 Lowe DJ, Blaauw M, Hogg AG, Newnham RM (2013) Ages of 24 widespread tephras
1337 erupted since 30,000 years ago in New Zealand, with re-evaluation of the timing and
1338 palaeoclimatic implications of the Lateglacial cool episode recorded at Kaipo bog. Quat
1339 Sci Rev 74:170-194
1340 Malfait W, Seifert R, Petitgirard S, Perrillat J-P, Mezouar M, Ota T, Nakamura E, Lerch P,
1341 Sanchez-Valle C (2014) Supervolcano eruptions driven by melt buoyancy in large
1342 silicic chambers. Nature Geosci 7:122-125
1343 Martin VM, Morgan DJ, Jerram DA, Caddick MJ, Prior DJ, Davidson JP (2008) Bang!
1344 Month-scale eruption triggering at Santorini Volcano. Science 321:1178
1345 Matthews NE, Pyle DM, Smith VC, Wilson CJN, Huber C, van Hinsberg V (2012) Quartz
1346 zoning and the pre-eruptive evolution of the ~340-ka Whakamaru magma systems,
1347 New Zealand. Contrib Mineral Petrol 163:87-107
1348 Miyashiro A (1974) Volcanic rock series in island arcs and active continental margins. Am J
1349 Sci 274:321-355
1350 Moore G, Vennemann T, Carmichael ISE (1998) An empirical model for the solubility of
1351 H_2O in magmas to 3 kilobars. Am Mineral 83:36-42

1352 Myers ML, Wallace PJ, Wilson CJN, Morter BK, Swallow EJ (2016) Prolonged ascent and episodic
1353 venting of discrete magma batches at the onset of the Huckleberry Ridge supereruption,
1354 Yellowstone. Earth Planet Sci Lett 451:285-297
1355 Nakamura M (1995) Continuous mixing of crystal mush and replenished magma in the
1356 ongoing Unzen eruption. Geology 23:807-810
1357 Nelson ST, Montana A (1992) Sieve-textured plagioclase in volcanic rocks produced by
1358 rapid decompression. Am Mineral 77:1242-1249
1359 Pallister JS, Hoblitt RP, Reyes AG (1992) A basalt trigger for the 1991 eruptions of Pinatubo
1360 volcano. Nature 356:426-428
1361 Pamukcu AS, Gualda GAR, Anderson AT (2012) Crystallization stages of the Bishop Tuff
1362 magma body recorded in crystal textures in pumice clasts. J Petrol 53:589-609
1363 Pamukcu AS, Gualda GAR, Bégué F, Gravley DM (2015) Melt inclusion shapes:
1364 timekeepers of short-lived giant magma bodies. Geology 43:947-950
1365 Pamukcu AS, Ghiorso MS, Gualda GAR (2016) High-Ti, bright-CL rims in volcanic quartz:
1366 a result of very rapid growth. Contrib Mineral Petrol 171:105
1367 Parmigiani A, Huber C, Bachmann O (2014) Mush microphysics and the reactivation of
1368 crystal-rich magma reservoirs. J Geophys Res: Solid Earth 119:6308-6322
1369 Pearce NJG, Westgate JA, Perkins WT (1996) Developments in the analysis of volcanic glass
1370 shards by laser ablation ICP–MS: quantitative and single internal standard multi-
1371 element methods. Quat Int 34-36:213-227
1372 Peppard BT, Steele IM, Davis AM, Wallace PJ, Anderson AT (2001) Zoned quartz
1373 phenocrysts from the rhyolitic Bishop Tuff. Am Mineral 86:1034-1052
1374 Price RC, Mortimer N, Smith IEM, Maas R (2015) Whole-rock geochemical reference data
1375 for Torlesse and Waipapa terranes, North Island, New Zealand. NZ J Geol Geophys
1376 58:213-228
1377 Putirka KD (2008) Thermometers and barometers for volcanic systems. In: Putirka KD,
1378 Tepley FJ (eds) Minerals, inclusions and volcanic processes. Reviews in Mineralogy
1379 and Geochemistry 69:61-120
1380 Reid MR (2008) How long does it take to supersize an eruption? Elements 4:23-28
1381 Reid MR, Vazquez JA Schmitt AK (2011) Zircon-scale insights into the history of a
1382 supervolcano, Bishop Tuff, Long Valley, California, with implications for the Ti-in-
1383 zircon geothermometer. Contrib Mineral Petrol 161:293-311

1384 Ridolfi F, Renzulli A, Puerini M (2010) Stability and chemical equilibrium of amphibole in
1385 calc-alkaline magmas: an overview, new thermobarometric formulations and
1386 application to subduction-related volcanoes. Contrib Mineral Petrol 160:45-66
1387 Rooyakkers SM (2015) A textural and micro-analytical study of quenched mafic inclusions
1388 from the Oruanui eruption, Taupo volcano, New Zealand. MSc thesis, Victoria
1389 University of Wellington
1390 Rowland JV, Wilson CJN, Gravley DM (2010) Spatial and temporal variations in magma-
1391 assisted rifting, Taupo Volcanic Zone, New Zealand. J Volcanol Geotherm Res 190:89-
1392 108
1393 Sauerzapf U, Lattard D, Burchard M, Engelman R (2008) The titanomagnetite-ilmenite
1394 equilibrium: new experimental data and thermo-oxybarometric application to the
1395 crystallization of basic to intermediate rocks. J Petrol 49:1161-1185
1396 Self S (1983) Large-scale phreatomagmatic silicic volcanism: a case study from New
1397 Zealand. J Volcanol Geotherm Res 17:433-469
1398 Self S (2006) The effects and consequences of very large explosive volcanic eruptions. Phil
1399 Trans Roy Soc Lond A364:2073-2097
1400 Self S, Sparks RSJ (1978) Characteristics of widespread pyroclastic deposits formed by the
1401 interaction of silicic magma and water. Bull Volcanol 41:196-212
1402 Shaw HR (1985) Links between magma-tectonic rate balances, plutonism, and volcanism. J
1403 Geophys Res 90:11275-11288
1404 Simon JI, Weis D, DePaolo DJ, Renne PR, Mundil R, Schmitt AK (2014) Assimilation of
1405 preexisting Pleistocene intrusions at Long Valley by periodic magma recharge
1406 accelerates rhyolite generation: rethinking the melting model. Contrib Mineral Petrol
1407 167:955
1408 Smith RL (1979) Ash-flow magmatism. In: Chapin CE, Elston WE (eds) Ash-flow Tuffs.
1409 Geol Soc Am Spec Pap 180:5-27
1410 Snyder D (2000) Thermal effects of the intrusion of basaltic magma into a more silicic
1411 magma chamber and implications for eruption triggering. Earth Planet Sci Lett
1412 175:257-273
1413 Sparks RSJ, Sigurdsson H, Wilson L (1977) Magma mixing: a mechanism for triggering acid
1414 explosive eruptions. Nature 267:315-318
1415 Sparks RSJ, Huppert HE, Turner JS (1984) The fluid dynamics of evolving magma
1416 chambers. Phil Trans R Soc Lond A310:511-534
1417 Sutton AN (1995) Evolution of a large silicic magma system: Taupo volcanic centre, New

1418 Zealand. Unpubl PhD thesis, The Open University, Milton Keynes, UK
1419 Sutton AN, Blake S, Wilson CJN (1995) An outline geochemistry of rhyolite eruptives from
1420 Taupo volcanic centre, New Zealand. J Volcanol Geotherm Res 68:153-175.
1421 Thomas JB, Watson EB, Spear FS, Shemella PT, Nayak SK, Lanzirotti A (2010) TitaniQ
1422 under pressure: the effect of pressure and temperature on the solubility of Ti in quartz.
1423 Contrib Mineral Petrol 160:743-759
1424 Thomas JB, Watson EB, Spear FS, Wark DA (2015) TitaniQ recrystallized: experimental
1425 confirmation of the original Ti-in-quartz calibrations. Contrib Mineral Petrol 169:27
1426 Tsuchiyama A (1985) Dissolution kinetics of plagioclase in the melt of the system diopside-
1427 albite-anorthite, and origin of dusty plagioclase in andesites. Contrib Mineral Petrol
1428 89:1-16
1429 Van Eaton AR, Wilson CJN (2013) The nature, origins and distribution of ash aggregates in a
1430 large-scale wet eruption deposit: Oruanui, New Zealand. J Volcanol Geotherm Res
1431 250:129-154
1432 Van Eaton AR, Herzog M, Wilson CJN, McGregor J (2012) Ascent dynamics of large
1433 phreatomagmatic eruption clouds: the role of microphysics. J Geophys Res 117:B03203
1434 Vandergoes MJ, Hogg AG, Lowe DJ, Newnham RM, Denton GH, Southon J, Barrell DJA,
1435 Wilson CJN, McGlone MS, Allan ASR, Almond PC, Petchey F, Dabell K,
1436 Dieffenbacher-Krall AC, Blaauw M (2013) A revised age for the Kawakawa/Oruanui
1437 Tephra, a key marker for the last Glacial Maximum in New Zealand. Quat Sci Rev
1438 74:195-201
1439 Venezky DY, Rutherford MJ (1999) Petrology and Fe-Ti oxide reequilibration of the 1991
1440 Mount Unzen mixed magma. J Volcanol Geotherm Res 89:213-230
1441 Wark DA, Watson EB (2006) TitaniQ: a titanium-in-quartz geothermometer. Contrib Mineral
1442 Petrol 152:743-754
1443 Wark DA, Hildreth W, Spear FS, Cherniak DJ, Watson EB (2007) Pre-eruption recharge of
1444 the Bishop magma system. Geology 35:235-238
1445 Waters LE, Lange RA (2015) An updated calibration of the plagioclase-liquid hygrometer-
1446 thermometer applicable to basalts through rhyolites. Am Mineral 100:2172-2184
1447 Wilson CJN (2001) The 26.5 ka Oruanui eruption, New Zealand: an introduction and
1448 overview. J Volcanol Geotherm Res 112:133-174
1449 Wilson CJN, Charlier BLA (2009) Rapid rates of magma generation at contemporaneous
1450 magma systems, Taupo volcano, New Zealand: insights from U-Th model-age spectra
1451 in zircons. J Petrol 50:875-907

1452 Wilson CJN, Blake S, Charlier BLA, Sutton AN (2006) The 26.5 ka Oruanui eruption, Taupo
1453 volcano, New Zealand: Development, characteristics and evacuation of a large rhyolitic
1454 magma body. J Petrol 47:35-69
1455 Wilson CJN, Gravley DM, Leonard GS, Rowland JV (2009) Volcanism in the central Taupo
1456 Volcanic Zone, New Zealand: tempo, styles and controls. In: Thordarson T, Self, S.,
1457 Larsen, G., Rowland, S.K., Hoskuldsson, A. (ed) Studies in Volcanology: The Legacy
1458 of George Walker. Spec Publ IAVCEI 2:225-247
1459 Wilson CJN, Seward TM, Charlier BLA, Allan ASR, Bello L (2012) A comment on: 'TitaniQ
1460 under pressure: the effect of pressure and temperature on the solubility of Ti in quartz',
1461 by Jay B. Thomas, E. Bruce Watson, Frank S. Spear, Philip T. Shemella, Saroj K.
1462 Nayak and Antonio Lanzirotti. Contrib Mineral Petrol 164:359-368
1463 Wotzlaw J-F, Bindeman IN, Stern RA, D'Abzac F-X, Schaltegger U (2015) Rapid
1464 heterogeneous assembly of multiple magma reservoirs prior to Yellowstone
1465 supereruptions. Sci Rep 5:srep14026
1466

Figure Captions

Fig. 1 Key volcanic and tectonic features of the Taupo area, located in the central North Island of New Zealand (see inset: TVZ – Taupo Volcanic Zone). Caldera structure and vent areas for phases 1 to 4 of the Oruanui eruption are from Wilson (2001). The NE-SW alignment of 'young' faults (<20 ka: Langridge et al. 2016) form the axis of regional extension in the modern TVZ. Dashed line marks the boundary between Taupo (T) and Maroa (M) volcanoes (Sutton et al. 1995). The stippled grey region encompasses the NE Dome magmatic system and associated biotite-rhyolite domes erupted in the last ~50 kyr (triangles – after Sutton et al. 1995). Modified from Wilson and Charlier (2009).

Fig. 2 **a** CaO versus Fe_2O_3 and **b** MgO versus SiO_2 data from fragments of pumice matrix glass in Oruanui high-silica rhyolite (HSR) and low-silica rhyolite (LSR) clasts (see text for definitions). All LSR clasts contain a bimodal glass compositions, the most evolved of which corresponds to that of the HSR clasts. The lack of a mixing/mingling relationship between the two groups of compositions suggests that the two rhyolite magmas only encountered each other syn-eruptively. **c** Ti versus Rb/Sr of (whole-rock) HSR pumices, HSR groundmass glass, and quartz-hosted melt inclusions. The majority of quartz-hosted melt inclusions record more evolved compositions (higher Rb/Sr ratio and lower concentrations of compatible elements) than the groundmass glass. Data sources: HSR pumice (Allan et al. 2012 and this paper); quartz-hosted melt inclusions (this paper); HSR groundmass glass from Allan et al. (2008) and Vandergoes et al. (2013). **d** Ti versus Rb/Sr of Oruanui rhyolite glasses. The HSR groundmass glass data here are from the distal fall deposits where single glass shards are large enough for analysis by LA-ICP-MS (>40 μm thick). The LSR glass values are from selvedges on, and melt inclusions in, plagioclase crystals in LSR clasts. Note the two distinct trends in LSR glass compositions.

Fig. 3 **a** Pictorial summary of the textural and zonation characteristics of orthopyroxene from Oruanui HSR clasts. See text for descriptions. White scale bars are 100 μm. **b** Pictorial summary of the textural and zonation characteristics of plagioclase crystals from Oruanui HSR clasts. See text for descriptions White scale bars are 100 μm.

1501 **Fig. 4** Representative examples of quartz zonation under cathodoluminescence (CL)
1502 imagery. **a** Multiply zoned crystals; **b** dark CL cores, bright CL rims; **c** bright CL
1503 cores, dark CL rims; **d** nominally unzoned. The black scale bars are 200 μm.
1504 **Fig. 5** Selected major element compositional data for plagioclase from **a** HSR and **b** LSR
1505 clasts, and **c**, **d** selected trace element data versus An content of plagioclase from
1506 HSR and LSR pumices. **e**, **f** Concentrations of Ti and Al versus mol % En for
1507 orthopyroxene from HSR and LSR clasts. **g, h** Concentrations of Mn and Zn versus
1508 Al content for orthopyroxenes from HSR and LSR clasts.
1509 **Fig. 6** Selected trace element concentration data for amphiboles from HSR and LSR
1510 clasts (symbols are as in Fig. 5). Data shown in panels **a**, **b** are plotted against the
1511 apparent crystallisation pressure as modelled by the Ridolfi et al. (2010) total-Al
1512 barometer and in panels **c**, **d** against the Eu/Eu* of the amphibole as a qualitative
1513 measure of evolution of the melt from which the amphibole grew. The origins of
1514 trends marked in each panel are discussed in the text.
1515 **Fig. 7** Selected whole-rock analytical data for single Oruanui mafic clasts, from this
1516 study, Rooyakkers (2015) and Wilson et al. (2006). **a** Plot of FeO*/MgO versus
1517 SiO_2 to show the two compositional groupings (calc-alkaline and tholeiitic: Wilson
1518 et al. 2006, dividing line from Miyashiro 1974). **b** New ICP-MS derived values for
1519 the Eu/Eu* ratio (Table 3 and Electronic Appendix 1). Note, in the tholeiitic group
1520 in particular, the positive Eu anomalies (i.e. Eu/Eu* >1) of most clasts, indicative
1521 of plagioclase accumulation.
1522 **Fig. 8** Comparisons of selected major element compositions of crystals from the mafic
1523 versus rhyolitic clasts. The yellow symbols identify analyses for which in-situ trace
1524 element data are available, whereas the orange symbols show analyses for which
1525 there is no corresponding trace element data. The higher spatial resolution of
1526 EPMA versus LA-ICP-MS was the main limiting factor in determining which
1527 crystals could be analysed for their trace element contents.
1528 **Fig. 9** Figure to illustrate the textural and compositional linkages between plagioclase
1529 crystals in the mafic clasts. BSE images of selected crystals are shown here to
1530 highlight some of the linkages that can be made between textures and composition,
1531 represented by a plot of FeO_t versus An content. Analysis spot points in the crystal
1532 images are marked with coloured stars that correspond to the equivalent coloured
1533 symbols in the central plot. The portion of the mafic clast dataset that plots at
1534 higher FeO_t contents at a given value of An (black and grey filled circles) consists

entirely of analyses of rapidly grown plagioclase, i.e. flash crystallised microlites in the groundmass and thin, quench-crystallised rims. The illustrated samples are labelled at the bottom of the images with CA and TH denoting crystals from calc-alkaline and tholeiitic clasts, respectively.

Fig. 10 Selected trace element compositional data of crystals from Oruanui juvenile mafic clasts. **a** Plagioclase. **b** Orthopyroxene from a representative evolved tholeiitic mafic clast (P574; SiO_2 = 62.4 wt.%). Note: only 35 of the 60 analyses by LA-ICP-MS on this sample included Al in the analytical scan. **c** Amphibole. The grey shaded regions in all panels show the corresponding compositional ranges from crystals from the HSR (blue) and LSR (green).

Fig. 11 **a** Fe-Ti oxide temperatures for equilibrium pairs (after Bacon and Hirschmann 1988) extracted from Oruanui juvenile mafic clasts. Temperatures are calculated using the model of Ghiorso and Evans (2008). Note the bimodality of the temperature estimates. The lower temperature group is assumed to represent pairs of oxides that were entrained from the crystal mush pile and/or during interactions with the rhyolite body. **b** Mean (± 2 sd) temperature determinations from two-pyroxene thermometry for 19 equilibrium opx-cpx pairs (i.e. K_D(Fe-Mg) = 1.09 ± 0.14). BK90 - Brey and Kohler (1990); P08 - Putirka (2008, his eqn. 37). **c** Fe-Ti oxide temperatures in the mafic clasts (from **a**) versus oxygen fugacity, with the respective fields for the LSR and HSR plotted.

Fig. 12 Ti versus Rb/Sr data for rhyolitic glasses (as annotated) and juvenile mafic clasts (whole-rock). The steeper trend observed in the LSR plagioclase selvedge and melt inclusion data are taken as indicating involvement of the tholeiitic mafic magma with the LSR glasses, and mixing controls on the tholeiitic whole-rock variations being with melts in the mush zone, not the melt-dominant body.

Fig. 13 Selected whole-rock analytical data for Oruanui felsic and mafic clasts. The tholeiitic group is split into three sub-groups on the basis of possible mixing trends. Chemical trends in the mafic groups overwhelmingly trend towards the LSR compositions and only 3 clasts (‘trend 3’) plausibly trend towards the volumetrically dominant HSR compositions.

Fig. 14 An example of a Fe-Ti diffusion modelling of a zoned magnetite crystal from clast P987 (calc-alkaline). In panels **a** and **b** the greyscale zonation across the crystal is examined to check for symmetry of the profile. Note the ‘flaring’ effect at the very edges of the crystal. In panel **c** a higher resolution portion of the crystal is selected

for modelling, and in panel **d** a model curve is fitted to the observed profile. In this example the crystal is interpreted to record a thermal perturbation in the final ~11 hours prior to quenching on eruption.

Fig. 15 Summary figure to show the time-scales of processes involved in the generation, accumulation and destruction of the Oruanui magma body as inferred from combined crystal-specific and field studies. Processes are numbered as follows.
1. Compositional characteristic of melt inclusions in xenocrystic quartz cores (Liu et al. 2006), radiogenic fingerprinting of xenocrystic blue-grey-cored plagioclase (Charlier et al. 2008), U-Pb zircon age fingerprinting of 'old' zircons (Charlier et al. 2010).
2. U-Th age spectra of zircons and crystal inheritance patterns with Oruanui precursor eruptions (Charlier et al. 2005; Wilson and Charlier 2009).
3. Processes identified by reconciliation of textural, thermobarometric and compositional data from Opx and amphibole (Allan et al. 2013). Timescales constrained as outlined in point 4 and in the supplementary material.
4. Fe-Mg diffusion timescales across the main core-rim boundaries in Opx (Allan et al. 2013). The equivalent boundary is texturally observed in plagioclase (this paper and Charlier et al. 2008).
5. Fe-Mg diffusion timescales from re-crystallised streaky, discontinuous zones in Opx (Allan et al. 2013)
6. Fe-Mg diffusion timescales from growth zones in Opx (Allan et al. 2013)
7. Crystal inheritance pathways, textural observation and disequilibrium textures (this paper)
8. Fe-Ti diffusion timescales in magnetite crystals (this paper)
9. Compositional relationships in matrix glass and crystals (this paper)
10. Compositional source fingerprinting and field constraints (Allan et al. 2012)
11. Li diffusion timescales in plagioclase and quartz (Charlier et al. 2012) and H_2O and CO_2 diffusion timescales from melt pockets (Liu et al. 2007)

Fig. 16 Schematised scaled cross section through the Taupo area to show the sources, depths and pathways for the various crystal and melt components represented in the Oruanui eruption products.

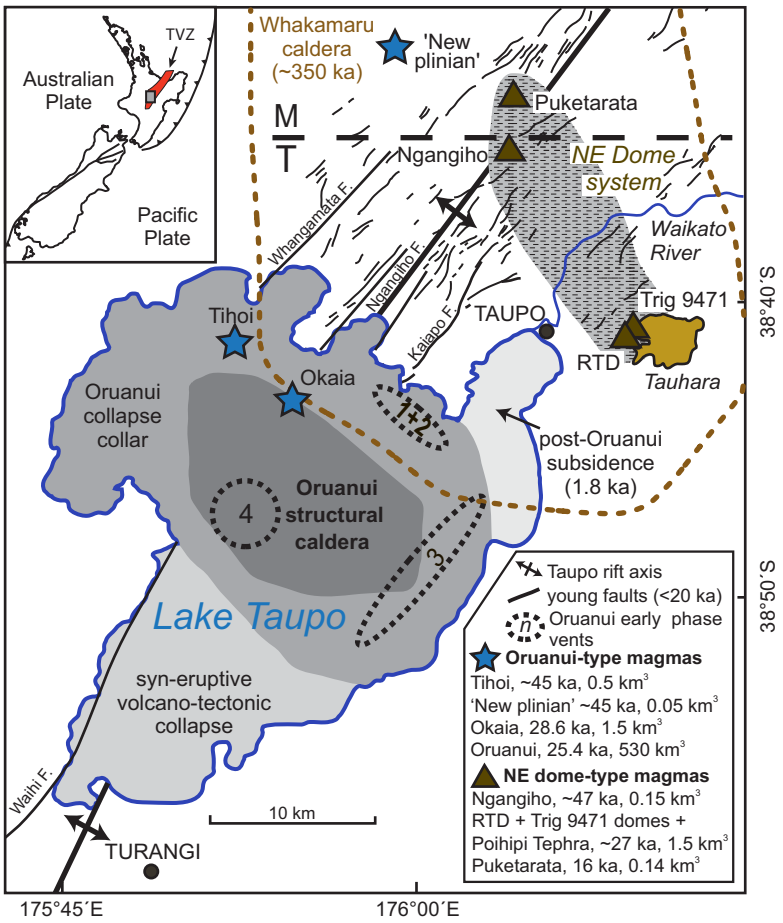

Allan et al. Figure 1

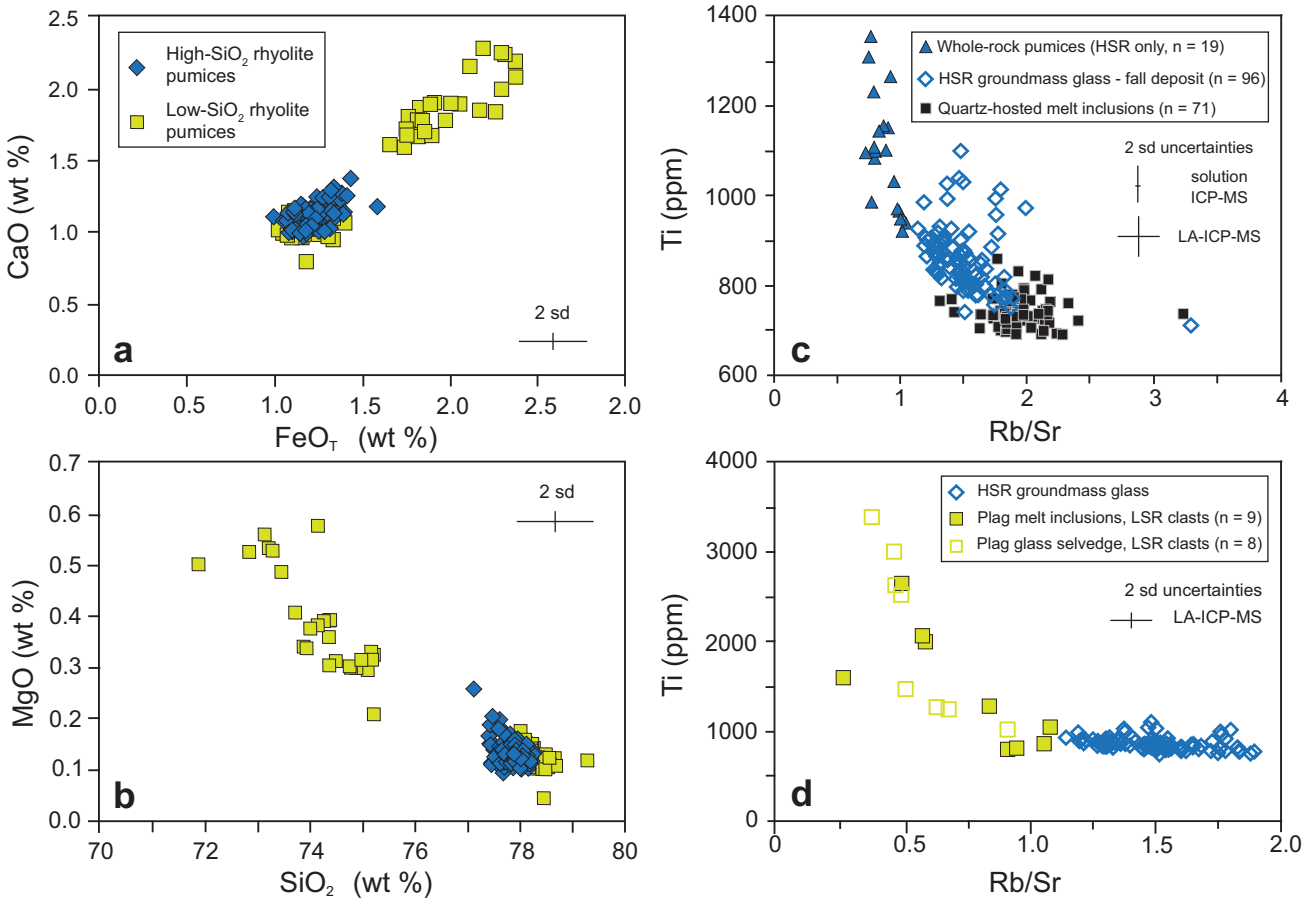

Allan et al. Figure 2

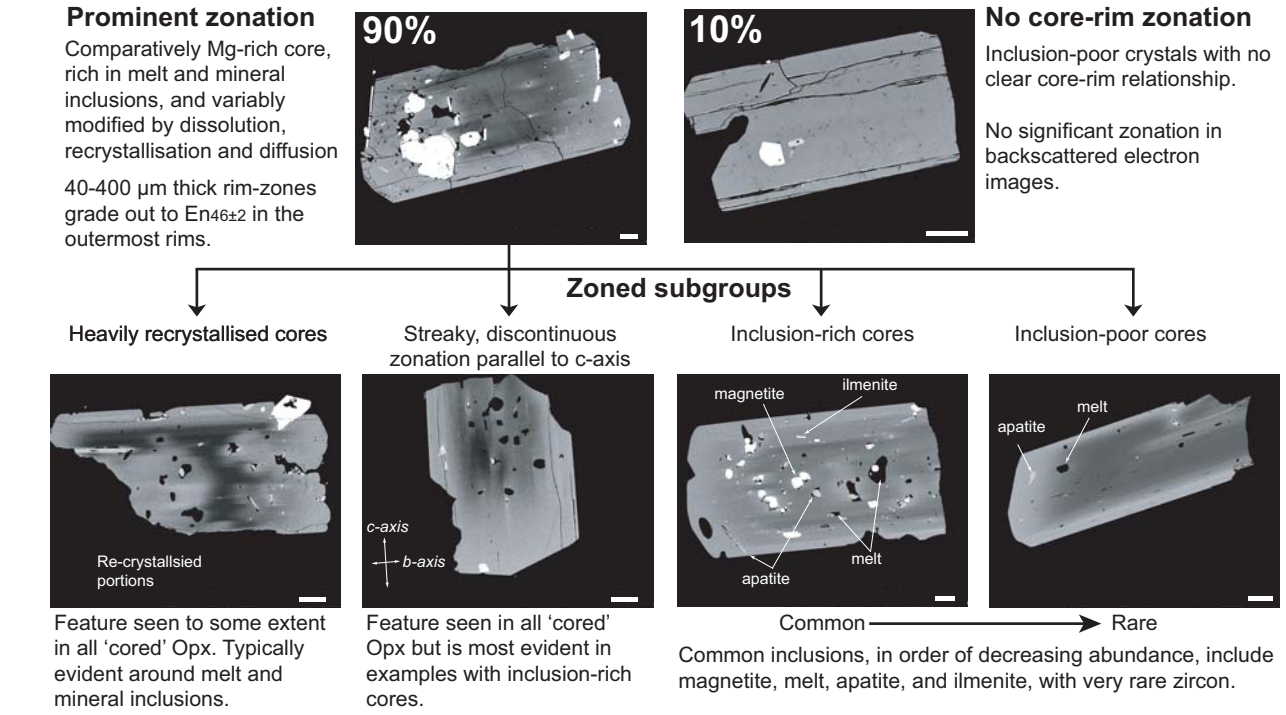

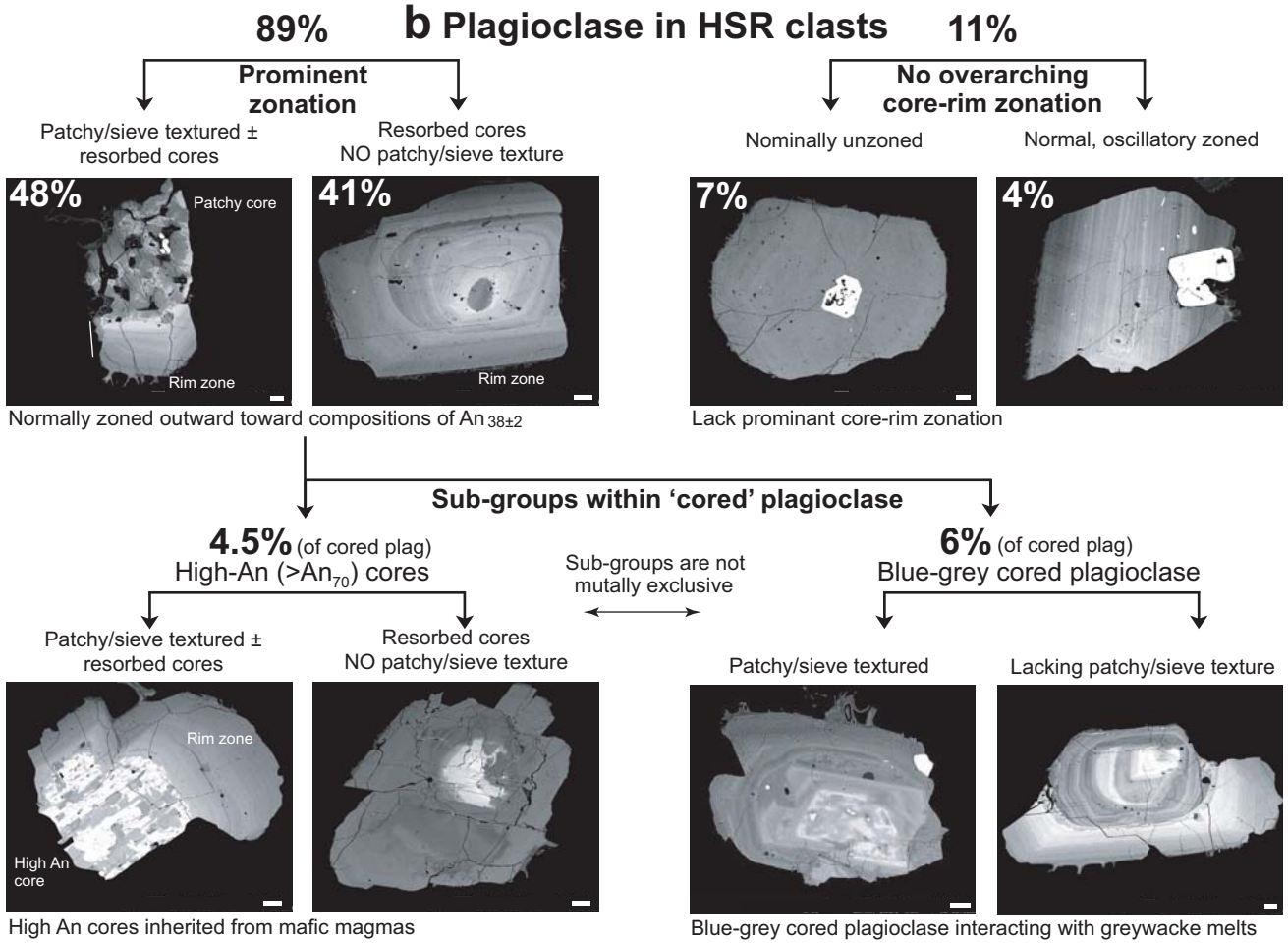

Allan et al. Figure 3

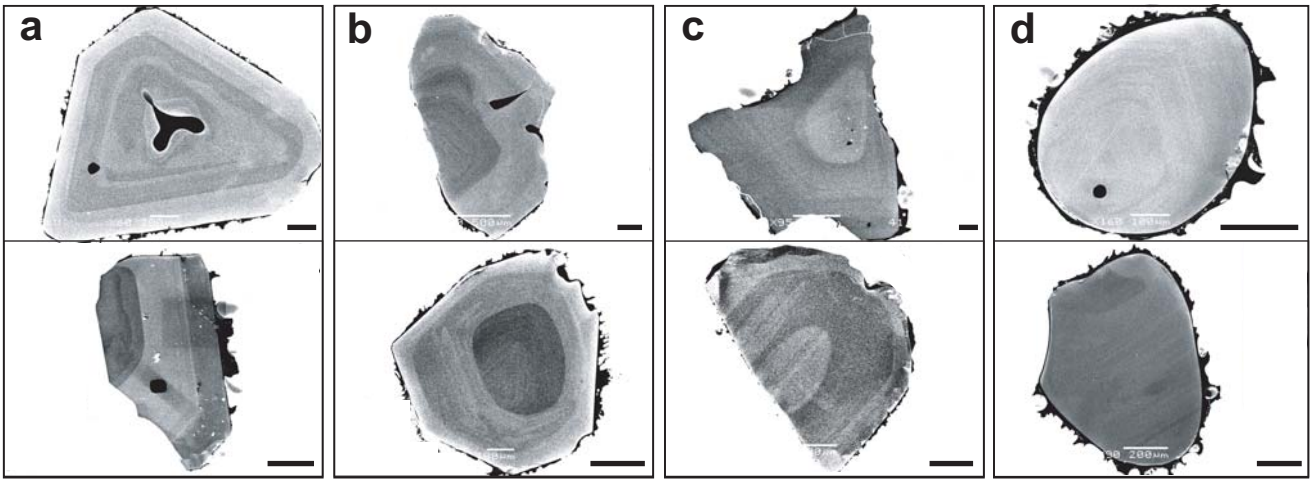

Allan et al. Figure 4

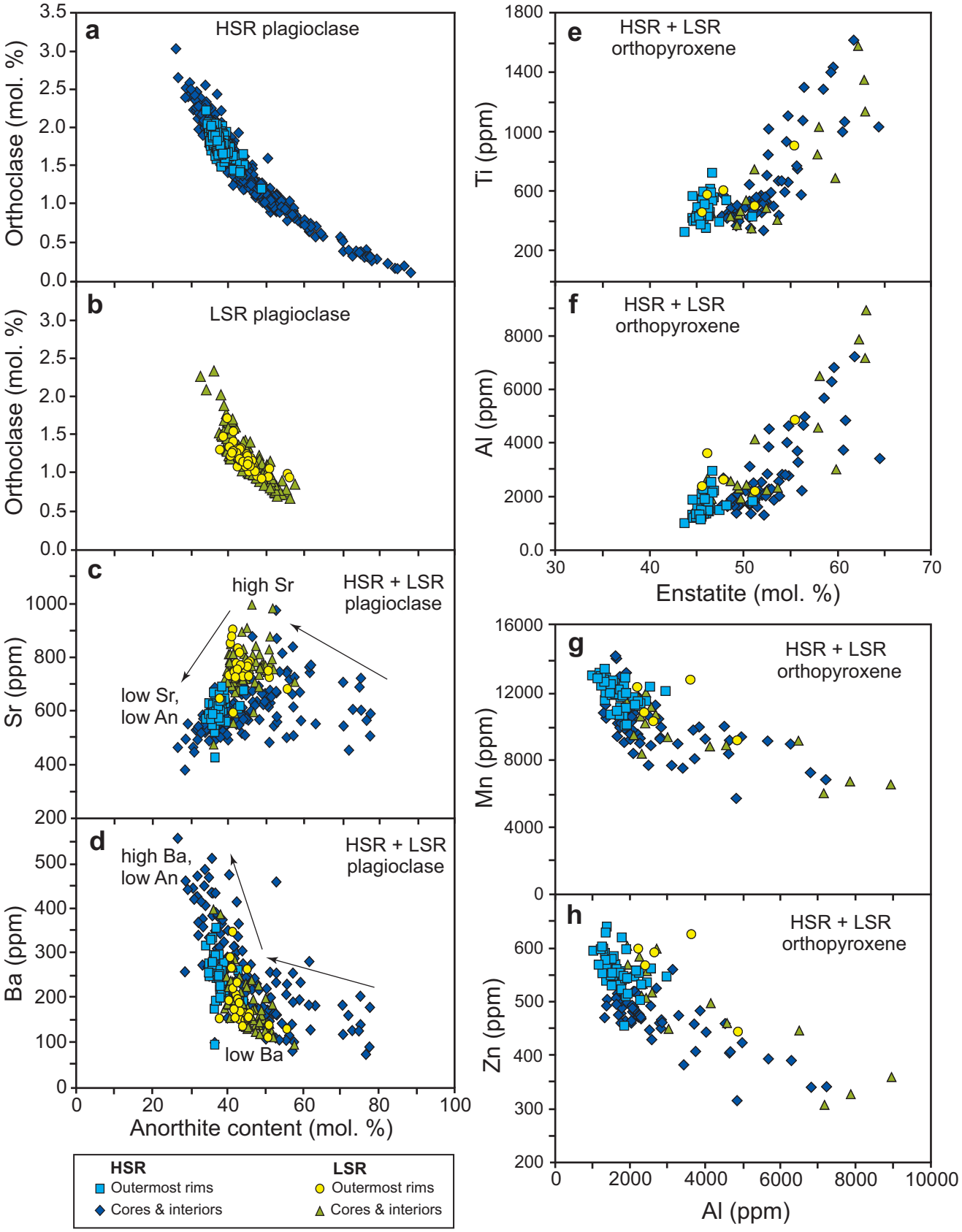

Allan et al. Figure 5

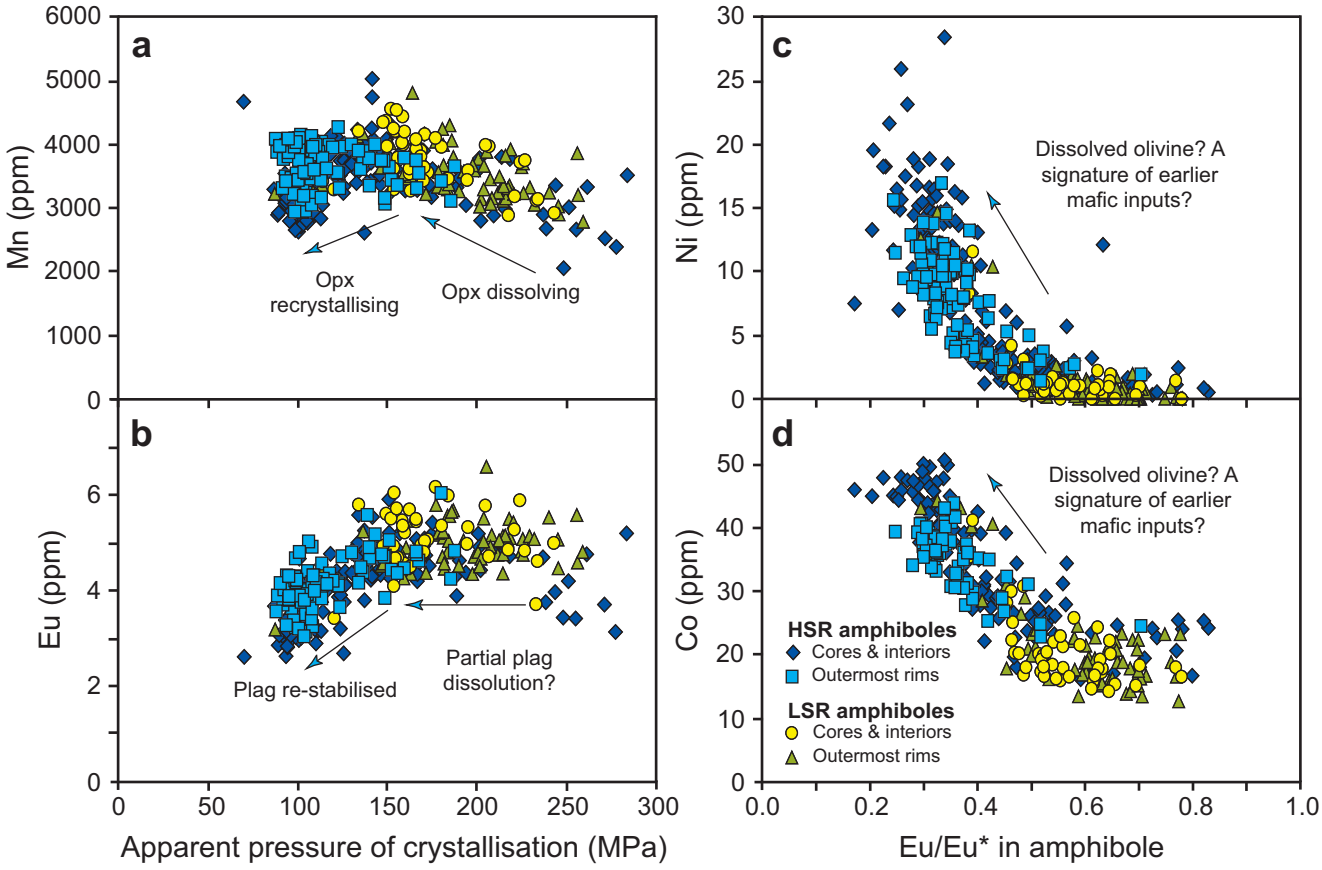

Allan et al. Figure 6

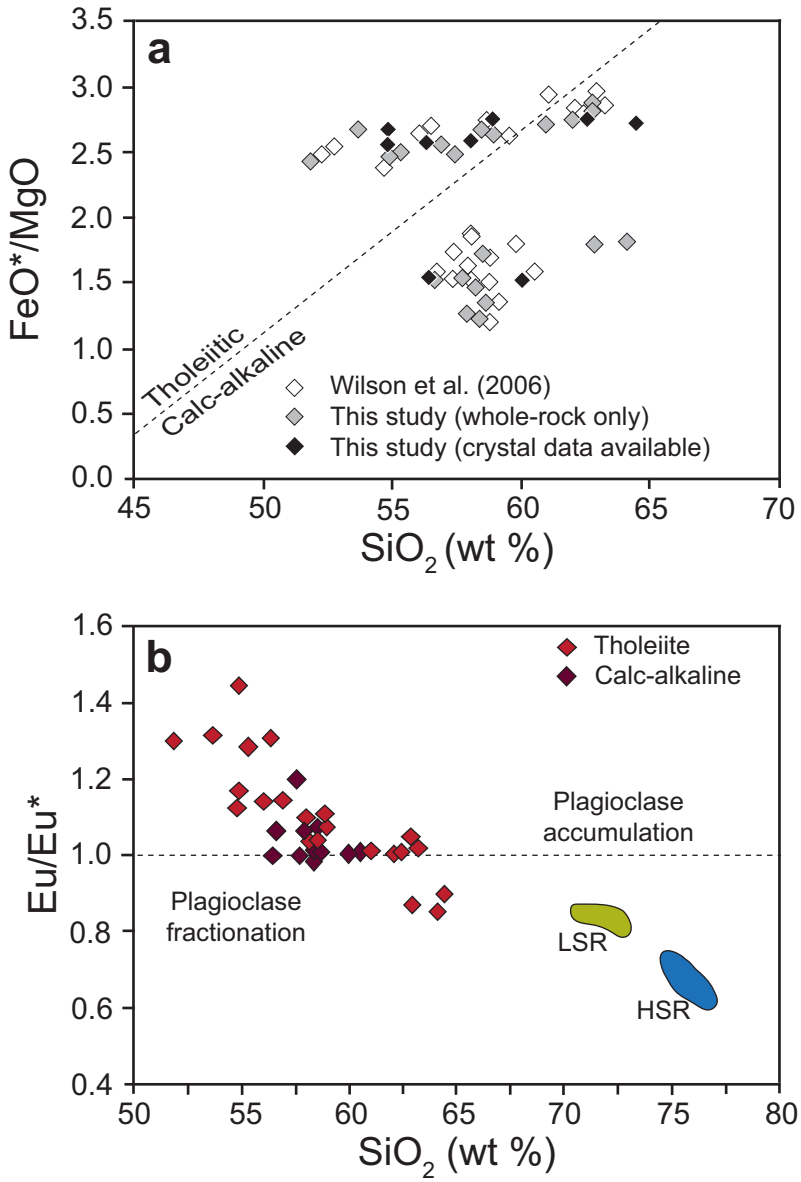

Allan et al. Figure 7

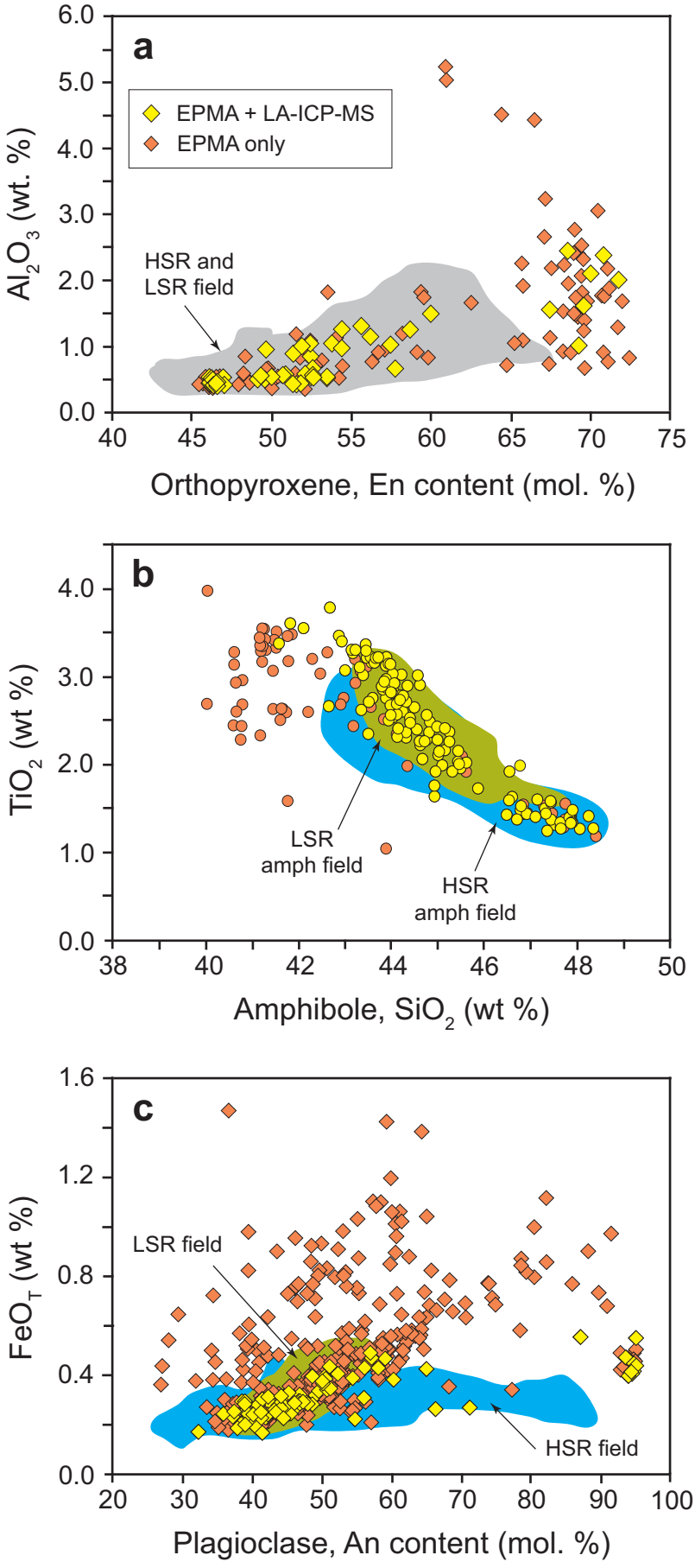

Allan et al Figure 8

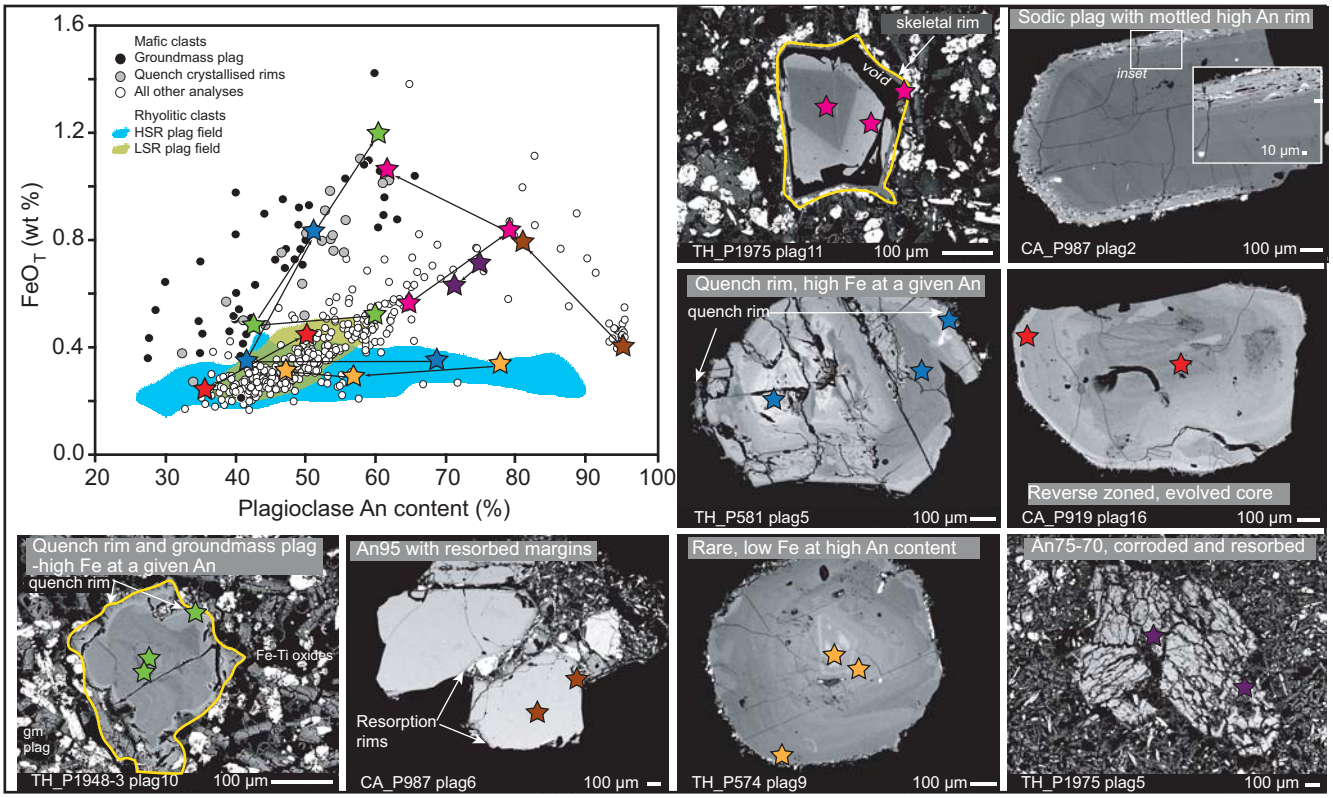

Allan et al. Figure 9

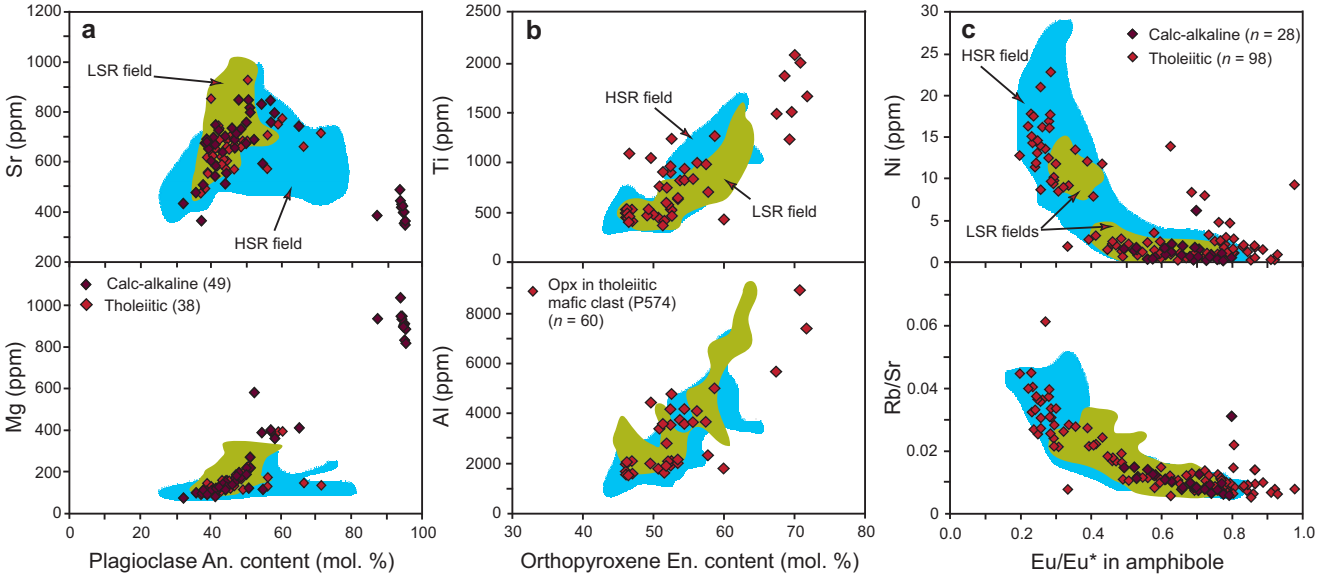

Allan et al. Figure 10

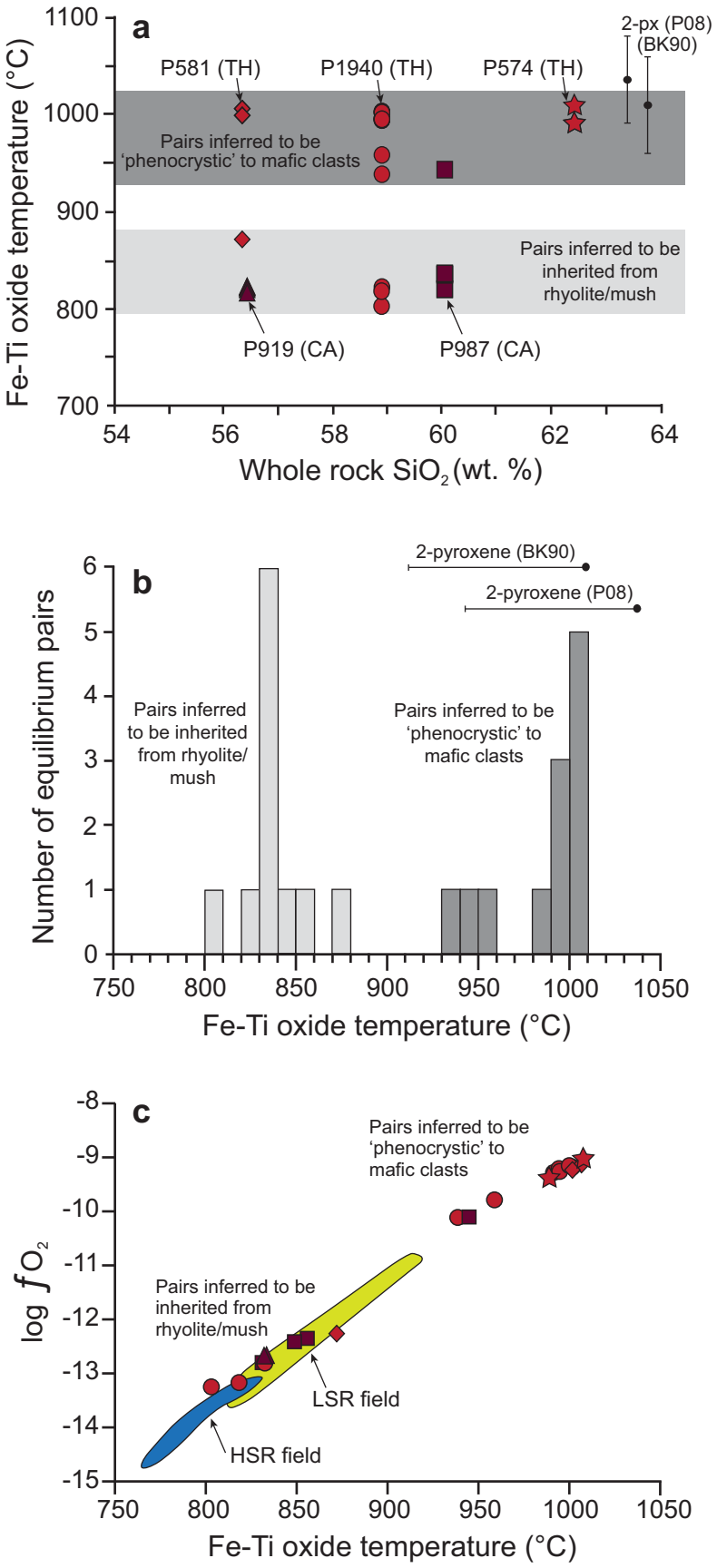

Allan et al. Fig. 11

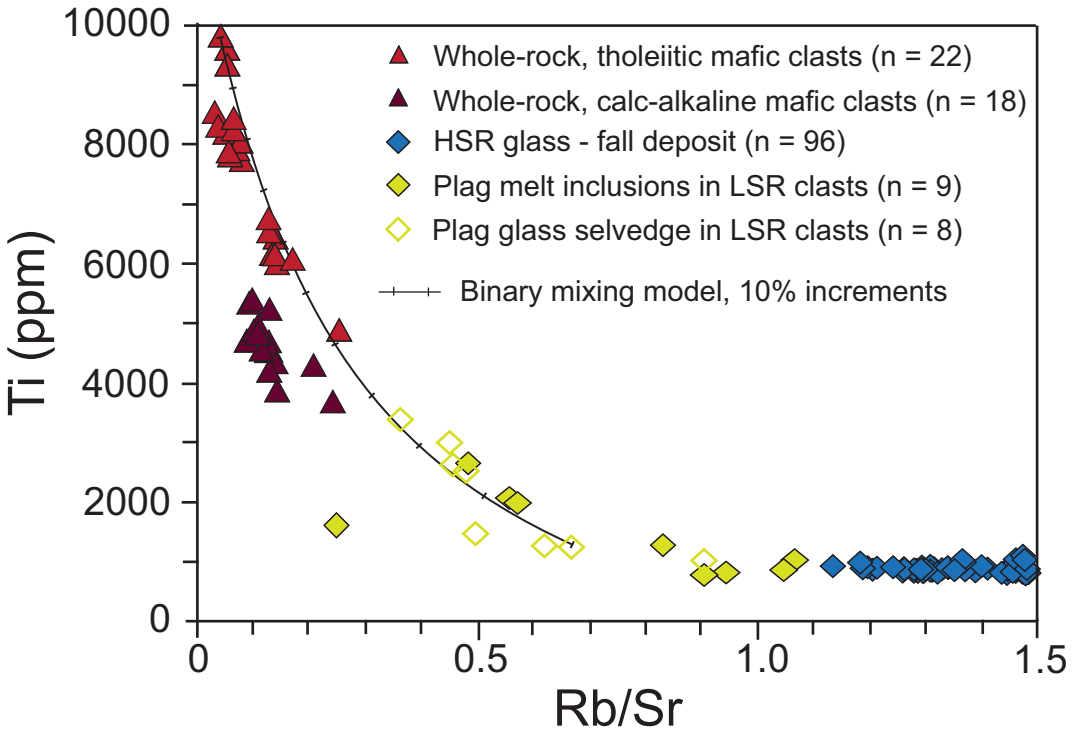

Allan et al. Figure 12

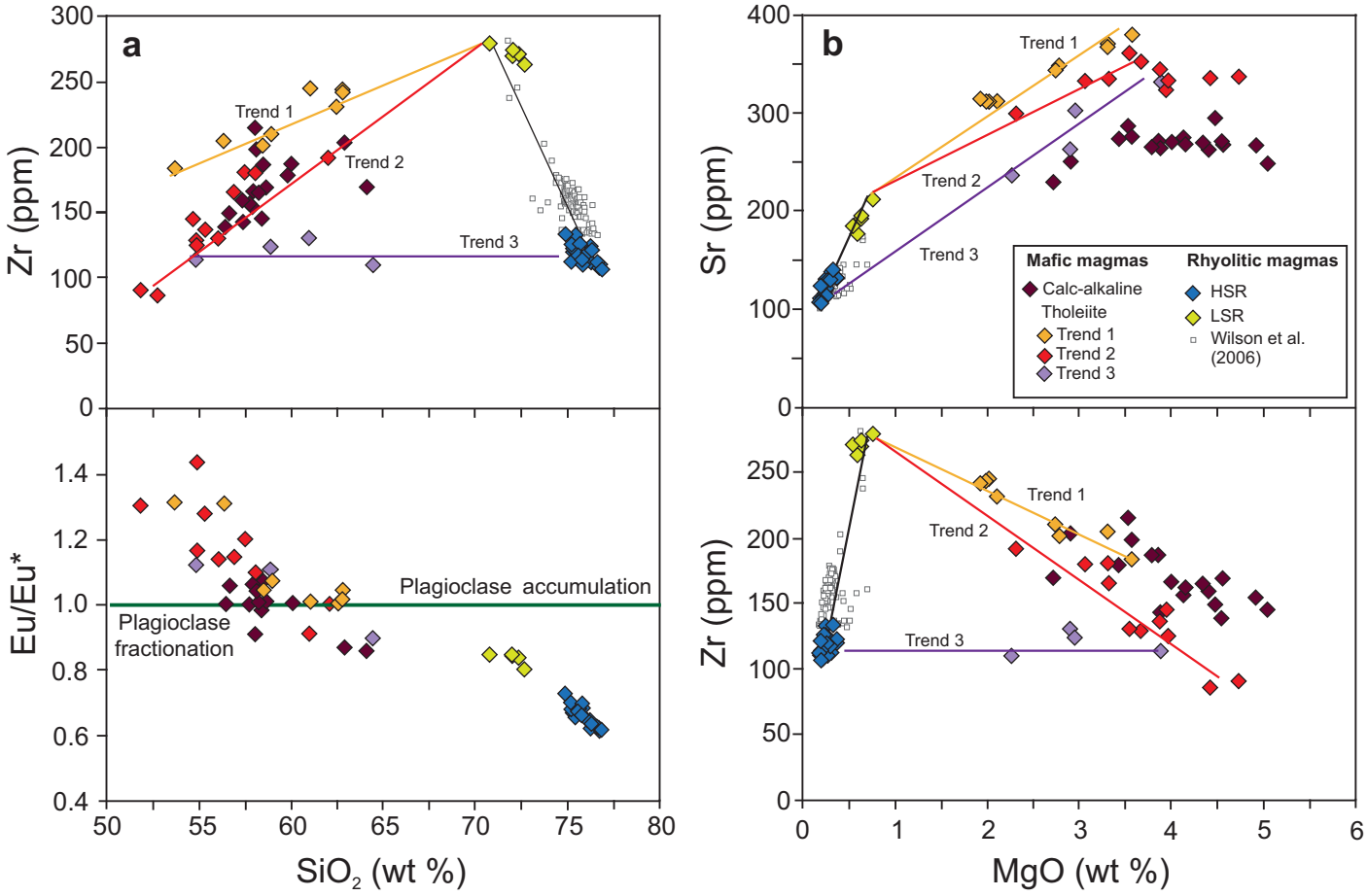

Allan et al. Figure 13

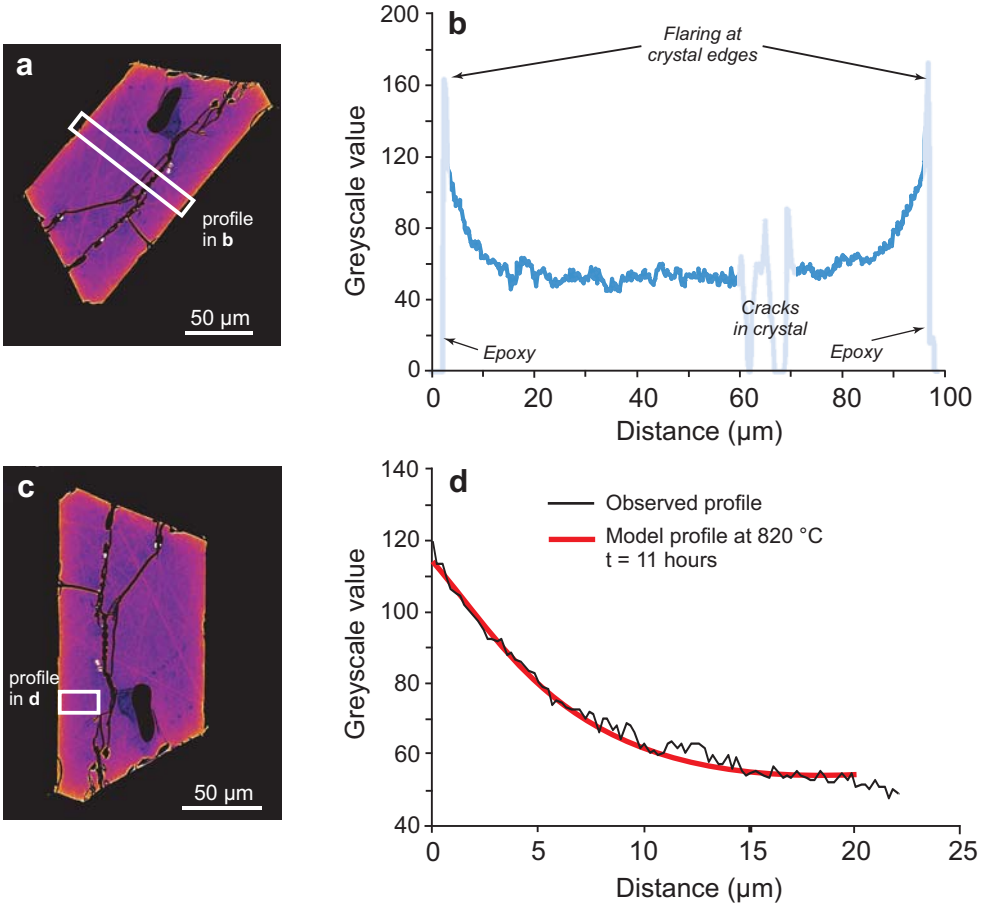

Allan et al. Figure 14

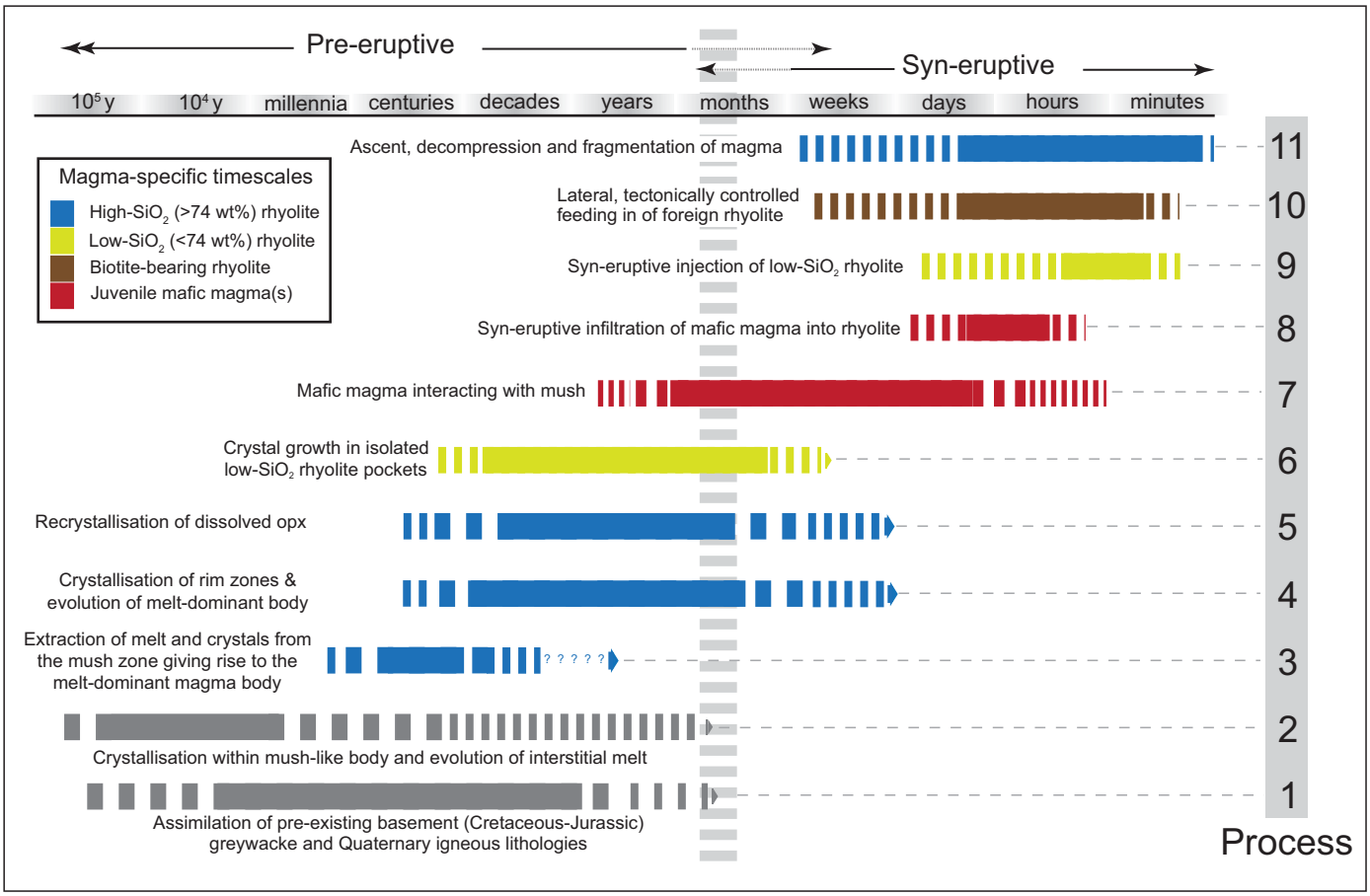

Allan et al. Figure 15

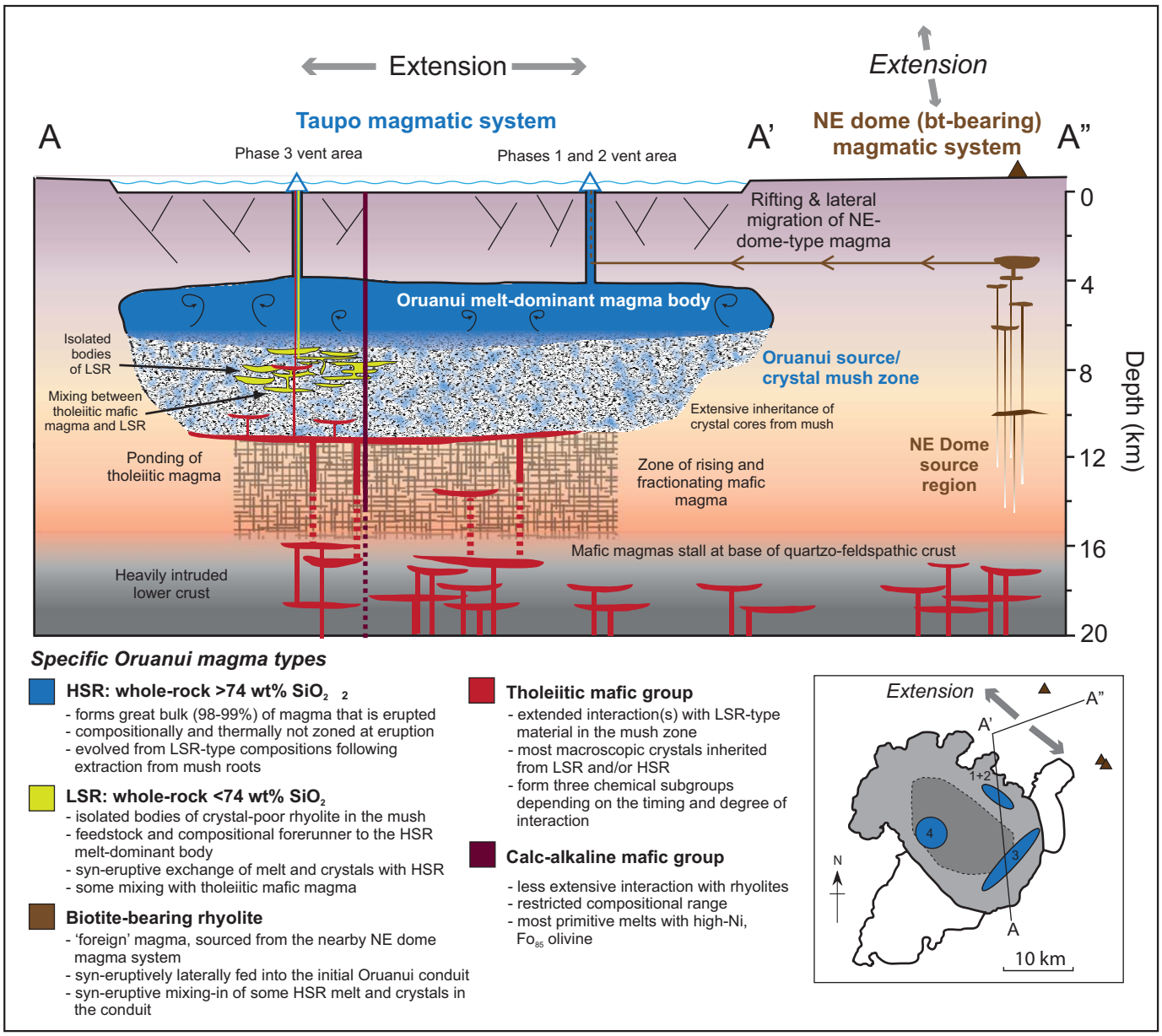

Allan et al. Figure 16

Table 1. Juvenile products of the Oruanui eruption.

Magma type	Features	Approx. magma volume	Abbreviations used in this paper	Key references
High-SiO_2 rhyolite	Whole-rock SiO_2 >74 wt%; 3-13% crystals; 64-73% plag, 15-21% qtz 7-8 % opx, 1.3-5% amph	525 km^3 (>98% of total)	HSR	Wilson et al. (2006); Liu et al. (2006); Allan et al. (2012, 2013)
Low-SiO_2 rhyolite	Whole-rock SiO_2 <74 wt%; 6% crystals; 67% plag, 0% qtz 8 % opx, 18% amph. Greatest abundance in deposits of phases 3 and 6.	0.5 km^3	LSR	Wilson et al. (2006); Allan et al. (2012, 2013)
Biotite-bearing	Biotite-bearing, 12-24% crystals, Rhyolite derived from an adjacent, independent magmatic system during phases 1 and 2	0.03 km^3	BtB	Sutton et al. (1995), Allan et al. (2012)
High-MgO rhyolite	Visually homogeneous pumices that fall along a trend of least evolved tholeiite mafic magma and HSR. Exceedingly rare as hand specimens	negl.	n/a	Wilson et al. (2006)
Streaky/mixed pumices	Streaky mixtures that fall along a trend of least evolved tholeiite mafic magma and HSR. Exceedingly rare as hand specimens	negl.	n/a	Wilson et al. (2006)
Juvenile mafic 1	Calc-alkaline trend, olivine common	1-3 km^3	CA	Wilson et al. (2006); Rooyakkers (2015); Rooyakkers et al. (in prep.)
Juvenile mafic 2	Tholeiitic trend, olivine rare	1-3 km^3	TH	Wilson et al. (2006); Rooyakkers (2015); Rooyakkers et al. (in prep.)

Note: plag = plagioclase, qtz = quartz, opx = orthopyroxene, amph = amphibole.

Table 2. Representative major (XRF) and trace element (ICP-MS) analyses of Oruanui rhyolitic clasts.

Sample no	P1957-3	P1959	P2110F	P1676	P2075	P2059	P1670	P2110C	P2110A	P2110B
Eruption phase	1	1	3	3	7	10	3	3	3	3
SiO_2	75.90	75.33	76.31	76.76	76.14	75.83	70.80	72.05	72.71	72.39
TiO_2	0.19	0.22	0.18	0.16	0.20	0.17	0.47	0.40	0.37	0.38
Al_2O_3	13.19	13.30	12.97	12.81	12.84	13.78	14.96	14.56	14.39	14.52
Fe_2O_3	1.72	1.92	1.69	1.60	1.81	1.68	3.25	2.93	2.82	2.87
MnO	0.06	0.06	0.06	0.05	0.06	0.05	0.10	0.10	0.09	0.09
MgO	0.27	0.37	0.26	0.22	0.26	0.20	0.76	0.63	0.59	0.55
CaO	1.65	1.81	1.55	1.42	1.50	1.41	2.81	2.38	2.25	2.33
Na_2O	4.04	4.07	3.70	3.68	4.11	3.87	4.35	4.21	3.91	4.05
K_2O	2.98	2.90	3.23	3.27	3.04	2.99	2.35	2.63	2.77	2.73
P_2O_5	0.02	0.03	0.04	0.03	0.04	0.02	0.13	0.10	0.09	0.10
LOI	2.82	3.41	3.44	3.36	2.76	3.39	3.91	4.14	4.63	4.47
SUM	96.80	96.15	95.80	96.62	96.63	95.96	95.68	95.14	94.58	94.63
FeO*/MgO	5.82	4.64	5.81	6.54	6.23	7.51	3.84	4.16	4.27	4.73
Li	31	28	13.7	13.5	36	29	16.6	15.5	26	26
Sc	5.7	6.8	5.9	5.3	6.7	6.0	11.9	10.2	10.6	10.1
Ti	1080	1350	1100	970	1270	1030	2820	2420	2300	2230
V	6.0	10.8	5.9	4.7	6.2	4.5	16.0	8.5	9.5	9.6
Cr	1.2	4.3	1.3	0.82	0.54	2.2	1.2	2.4	4.5	3.4
Co	1.3	2.0	1.8	1.2	1.2	1.0	-	-	-	-
Ni	-	-	-	-	1.5	1.3	-	-	-	-
Cu	4.5	4.6	3.1	3.1	3.1	4.1	2.9	4.2	5.8	4.6
Zn	56	62	63	58	46	45	76	79	66	65
Ga	15.2	15.6	15.3	14.8	14.8	15.2	17.8	17.5	17.3	17.1
Rb	102	102	108	110	105	103	72	76	83	79
Sr	129	133	122	113	114	108	213	193	178	186
Y	23	24	24	23	24	22	28	28	28	27
Zr	114	123	112	108	120	114	280	270	264	272
Nb	6.5	6.7	6.6	6.4	7.3	7.0				
Cs	5.5	5.4	6.1	6.0	4.7	4.4	3.8	4.0	4.4	3.4
Ba	628	604	646	614	658	672	510	539	565	545
La	22	22	23	22	23	21	21	22	21	21
Ce	44	44	47	45	47	45	44	46	45	45
Pr	4.9	5.0	5.2	5.1	5.1	4.8	5.3	5.5	5.3	5.3
Nd	17.8	18.5	19.1	18.5	18.8	17.4	21	22	21	21
Sm	3.6	3.8	3.9	3.8	3.9	3.5	4.6	4.7	4.6	4.5
Eu	0.82	0.84	0.80	0.78	0.82	0.77	1.3	1.3	1.2	1.3
Gd	3.7	3.9	3.9	3.8	3.9	3.6	4.9	4.9	4.7	4.6
Tb	0.57	0.60	0.60	0.57	0.60	0.55	0.76	0.76	0.74	0.72
Dy	3.7	3.8	3.9	3.7	3.9	3.5	4.8	4.8	4.7	4.6
Ho	0.78	0.80	0.80	0.78	0.81	0.74	1.0	1.0	1.0	0.95
Er	2.4	2.5	2.4	2.4	2.5	2.2	3.0	3.0	3.0	2.9
Tm	0.36	0.38	0.37	0.36	0.38	0.34	0.45	0.45	0.45	0.44
Yb	2.5	2.6	2.6	2.6	2.6	2.4	3.0	3.0	3.1	3.0
Lu	0.39	0.40	0.40	0.39	0.39	0.36	0.47	0.47	0.47	0.46
Hf	3.5	3.6	3.4	3.4	3.6	3.6	6.4	6.5	6.4	6.3
Pb	12.7	12.6	13.2	13.1	13.1	13.7	9.9	10.8	11.4	11.0
Th	10.7	10.7	11.1	11.0	10.6	11.3	7.4	8.0	8.6	8.0
U	2.4	2.4	2.5	2.6	2.4	2.4	1.8	1.9	2.0	1.9
Rb/Sr	0.79	0.76	0.88	0.97	0.92	0.95	0.34	0.39	0.47	0.42
Eu/Eu*	0.68	0.67	0.62	0.62	0.65	0.66	0.85	0.84	0.80	0.84

Table 3. Representative major (XRF) and trace element (ICP-MS) analyses of Oruanui juvenile mafic clasts.

Sample no	P554	P1975	P581	P1974	P574	P1976	P1643	P919	P1664	P987
Group	TH	TH	TH	TH	TH	TH	CA	CA	CA	CA
SiO_2	52.27	54.83	56.52	58.05	62.43	64.47	56.66	56.74	57.90	60.53
TiO_2	1.44	1.31	1.68	1.24	1.02	0.79	0.79	0.80	0.67	0.78
Al_2O_3	16.92	16.54	17.67	16.71	16.59	14.89	17.84	17.25	17.74	16.61
Fe_2O_3	12.60	11.04	9.60	8.81	6.30	6.86	7.56	7.83	6.91	6.53
MnO	0.19	0.17	0.18	0.16	0.15	0.12	0.14	0.15	0.12	0.14
MgO	4.57	3.89	3.20	3.07	2.03	2.27	4.47	4.45	4.92	3.70
CaO	8.13	7.62	5.98	6.53	5.23	4.94	8.31	8.69	7.44	6.59
Na_2O	3.28	3.51	4.30	4.06	4.46	3.70	3.15	3.06	3.16	3.67
K_2O	0.48	0.77	0.74	0.96	1.40	1.78	0.85	0.83	0.97	1.22
P_2O_5	0.11	0.33	0.14	0.41	0.40	0.19	0.23	0.20	0.17	0.22
LOI	1.80	0.80	2.22	1.01	1.22	1.47	0.91	0.76	1.23	1.46
SUM	100.30	99.31	100.32	99.07	99.36	98.55	99.06	98.57	98.78	99.18
FeO*/MgO	2.48	2.55	2.70	2.58	2.79	2.72	1.52	1.58	1.26	1.58
Li	10.7	14.7	13.4	16.0	11.7	23.1	14.5	13.5	12.8	15.0
Sc	40	32	28	28	21	21	28	30	25	23
Ti	8550	7820	9610	7740	6440	4890	4710	4710	4200	4350
V	364	272	123	163	78	159	154	162	122	102
Cr	4.7	3.8	0.76	3.1	1.8	8.6	102	111	100	85
Co	28	22	9.6	13.7	7.5	14.1	21	21	22	15
Ni	3.6	2.3	2.0	1.7	1.9	2.0	21	18.4	41	20
Cu	12.9	14.3	6.0	6.8	4.8	13.5	14.6	14.5	13.8	8.6
Zn	106	94	107	93	83	69	74	75	81	74
Ga	21	20	22	20	20	17.9	18.2	17.9	17.6	18.0
Rb	10.6	19.7	20	27	44	60	26	24	35	38
Sr	338	332	367	333	312	237	295	271	267	271
Y	17.3	20	20	24	27	22	20	20	19.3	22
Zr	90	114	204	180	231	110	149	138	154	187
Nb	2.7	3.5	6.2	5.1	6.8	5.5	4.0	3.8	4.2	5.1
Cs	0.41	0.98	0.83	1.3	1.8	3.1	0.96	0.96	1.7	1.5
Ba	152	200	279	253	365	405	313	212	285	302
La	5.1	9.3	8.3	11.9	16.3	15.7	10.0	9.6	9.7	12.7
Ce	14.5	21	19.6	27	36	33	23	22	22	28
Pr	1.8	2.9	2.5	3.6	4.5	3.9	3.0	2.8	2.8	3.5
Nd	8.6	12.8	11.0	16.0	19.3	15.9	12.9	12.4	11.9	15.1
Sm	2.5	3.2	3.0	4.0	4.6	3.5	3.2	3.1	2.8	3.7
Eu	1.1	1.3	1.4	1.5	1.5	1.1	1.2	1.1	1.1	1.3
Gd	2.8	3.5	3.4	4.4	5.0	3.7	3.6	3.5	3.2	3.9
Tb	0.48	0.55	0.56	0.68	0.74	0.58	0.56	0.54	0.51	0.61
Dy	3.1	3.5	3.7	4.3	4.7	3.7	3.6	3.5	3.3	3.9
Ho	0.67	0.73	0.76	0.87	0.97	0.77	0.75	0.73	0.69	0.81
Er	1.9	2.1	2.2	2.5	2.8	2.3	2.2	2.1	2.0	2.4
Tm	0.27	0.31	0.32	0.36	0.40	0.34	0.32	0.31	0.30	0.34
Yb	1.8	2.0	2.2	2.4	2.7	2.3	2.1	2.1	2.0	2.3
Lu	0.27	0.29	0.32	0.36	0.41	0.35	0.32	0.32	0.31	0.35
Hf	2.3	2.7	4.6	4.0	5.2	3.0	3.4	3.2	3.5	4.2
Pb	3.4	6.4	8.2	4.9	7.0	14.4	4.0	4.1	5.2	5.9
Th	1.5	2.1	3.1	3.0	4.8	6.2	2.8	2.7	3.4	4.0
U	0.38	0.53	0.73	0.73	1.2	1.4	0.67	0.65	0.84	0.97
Rb/Sr	0.03	0.06	0.05	0.08	0.14	0.25	0.09	0.09	0.13	0.14
Eu/Eu*	1.30	1.13	1.31	1.10	1.01	0.90	1.06	1.00	1.07	1.01

Table 4. Summary of estimates for the pre-eruptive temperature of the Oruanui melt-dominant magma body yielded by various mineral equilibrium based techniques

Estimates of outermost rim crystallisation temperatures (T°C)	Number of estimates	Mean temp (°C)	Temp range (°C)	Modal values	Model details and/or parameters
HSR magma					
Plag-melt (rims)	158	787	783 - 797		Putirka (2008), eqn 24a, matrix glass and 5.5 wt% melt H_2O
Opx-melt (rims)	222	785	779 - 793		Putirka (2008), eqn 28a, matrix glass and 5.5 wt% melt H_2O
Amphibole compositions (rims)	121	784	751 - 851	770-780	Ridolfi et al. (2010) model
Fe-Ti oxides	378	796	765 - 836	790	Ghiorso and Evans (2008) model
LSR magma					
Plag-melt (rims)	47	831		820-840	Putirka (2008), eqn 24a, matrix glass and 6 wt% melt H_2O
Opx-melt (rims)	49	830		820-840	Putirka (2008), eqn 28a, matrix glass and 6 wt% melt H_2O
Amphibole compositions (rims)	59	837	783-903	820-850	Ridolfi et al. (2010) model
Fe-Ti oxides	61	840	812-910	840	Ghiorso and Evans (2008) model

Table 5. Summary of oxygen fugacity and melt H_2O estimates for the final pre-eruptive conditions in the Oruanui HSR and LSR magmas.

Estimates of oxygen fugacity (ΔNNO)	n	Mean (ΔNNO)	Range (ΔNNO)	Model details and/or parameters
HSR magma				
Fe-Ti oxides	379	-0.20	-0.52 to 0.03	Ghiorso and Evans (2008)
Amphibole rims	121	0.90	0.40 to 1.20	Ridolfi et al. (2010)
LSR magma				
Fe-Ti oxides	59	0.5	0.2-0.8	Ghiorso and Evans (2008)
Amphibole rims	59	0.5	0.2-0.8	Ridolfi et al. (2010)
Estimates of H_2O melt (wt %)		Mean (wt %)	Range	Model details and/or parameters
HSR magma				
Amphibole rims	121	5.5	5.0 - 6.2	Ridolfi et al. (2010) model
Quartz-host melt inclusions	66	4.5	3.8 - 5.1	Liu et al. (2006), H_2O in quartz-hosted melt inclusions measured by FTIR
Empirical H_2O solubility model	-	5.2	3.9 - 6.6	Moore et al. (1998), model run at 796 °C and 90-240 MPa, mean value at 150 MPa
Glass H_2O by difference	141	4.5	0.6 - 7.4	Difference from 100 wt% of raw EPMA totals for pumice matrix glass
Plag-melt equilibrium		4.6		Anorthite-method of Housh and Luhr (1991), reported in Wilson et al. (2006)
Plag-melt equilibrium		6.2		Albite-method of Housh and Luhr (1991), reported in Wilson et al. (2006)
Plag-melt equilibrium		5.5		Method of Waters and Lange (2015) with 790 °C and outer rim values of $An_{38\pm2}$
LSR magma				
Amphibole rims	59	6.0	5.6-6.5	Ridolfi et al. (2010) model
Plag-melt equilibrium		5.3		Method of Waters and Lange (2015) with 840 °C and outer rim values of An_{44}